ENVIRONMENTAL RESEARCH
CLIMATE

PAPER

AMOC weakening in response to global and regional reductions in aerosol emissions

OPEN ACCESS

RECEIVED
26 January 2026

REVISED
9 April 2026

ACCEPTED FOR PUBLICATION
23 April 2026

PUBLISHED
15 May 2026

Robert J Allen[1,*], Timothy Carson[1], Wei Liu[1], Laura J Wilcox[2], Bjørn H Samset[3], Sharar Ahmadi[2], Annica M L Ekman[4], Maxwell T Elling[5,6], Luke Fraser-Leach[7], Paul Griffiths[8], James Keeble[9], Tsuyoshi Koshiro[10], Paul Kushner[7], Anna Lewinschal[4], Molly MacRae[11,12], Risto Makkonen[13], Joonas Merikanto[13], Pierre Nabat[14], Larissa Nazarenko[15,16], Declan O'Donnell[13], Naga Oshima[10], David Paynter[17], Geeta Persad[18], Steven T Rumbold[2], Neil Swart[19], Toshihiko Takemura[20], Kostas Tsigaridis[15,16], Knut von Salzen[19,21], Daniel M Westervelt[16,22] and Taufiq Hassan[23]

[1] Department of Earth and Planetary Sciences, University of California, Riverside, United States of America
[2] National Centre for Atmospheric Science, University of Reading, Reading, United Kingdom
[3] CICERO Center for International Climate Research, Oslo, Norway
[4] Department of Meteorology, Stockholm University, Bolin Centre for Climate Research, Stockholm, Sweden
[5] Department of Atmospheric and Oceanic Sciences, University of Colorado Boulder, Boulder, United States of America
[6] Cooperative Institute for Research in Environmental Sciences, University of Colorado Boulder, Boulder, United States of America
[7] Department of Physics, University of Toronto, Toronto, Canada
[8] School of Chemistry, University of Bristol, Bristol, United Kingdom
[9] Lancaster Environment Centre, Lancaster University, Lancaster, United Kingdom
[10] Meteorological Research Institute, Japan Meteorological Agency, Ibaraki, Japan
[11] Centre for Environmental Data Analysis, Science & Technology Facilities Council, Rutherford Appleton Laboratory, Didcot, United Kingdom
[12] Department of Meteorology, University of Reading, Reading, United Kingdom
[13] Finnish Meteorological Institute, Helsinki, Finland
[14] Météo-France, CNRS, University Toulouse, CNRM, Toulouse, France
[15] Center for Climate Systems Research, Columbia University, Palisades, United States of America
[16] NASA Goddard Institute of Space Studies, New York, NY, United States of America
[17] NOAA/Geophysical Fluid Dynamics Laboratory, Princeton, NJ, United States of America
[18] Department of Earth and Planetary Sciences, The University of Texas at Austin, Austin, TX, United States of America
[19] Canadian Centre for Climate Modelling and Analysis, Environment and Climate Change Canada, Victoria, BC, Canada
[20] Research Institute for Applied Mechanics, Kyushu University, Fukuoka, Japan
[21] Department of Atmospheric and Climate Science, University of Washington, Seattle, United States of America
[22] Lamont-Doherty Earth Observatory, Columbia Climate School, New York, NY, United States of America
[23] California Air Resources Board, Sacramento, CA, United States of America
* Author to whom any correspondence should be addressed.

E-mail: rjallen@ucr.edu

Keywords: aerosols, Atlantic Meridional Overturning Circulation, Regional Aerosol Model Intercomparison Project

Supplementary material for this article is available online

Abstract

In response to continued greenhouse gas (GHG) increases, the Atlantic Meridional Overturning Circulation (AMOC) is expected to weaken through the 21st century. However, AMOC impacts associated with efforts to improve air quality are less well understood. Here, eight models from the Regional Aerosol Model Intercomparison Project are examined to quantify mid-21st century AMOC changes resulting from global and regional anthropogenic aerosol and precursor gas (AA) emissions reductions (industrial and biomass burning), by comparing strong air pollution control shared socioeconomic pathway (SSP1-2.6) to a baseline with weak air pollution control (SSP3-7.0). Global AA reductions and subsequent warming yield multi-model mean AMOC weakening of 6% (-0.98 ± 0.40 Sv; 1 Sv $= 10^6$ m^3 s^{-1}) by the last 12 years of the simulation (2039–2050). This is ⅓ of the magnitude of the corresponding weakening associated with the high GHG emissions scenario SSP3-7.0. Of the regional perturbations, combined North American and European AA reductions drive the largest AMOC weakening, followed by combined African and Middle

Eastern reductions and then East Asian reductions, with South Asian reductions yielding non-significant weakening. Across these experiments, AMOC weakening is significantly correlated with the North Atlantic Ocean aerosol effective radiative forcing ($r = -0.95$) and aerosol optical depth response ($r = 1.0$). AMOC weakening under AA reductions is associated with a thermally driven reduction in buoyancy in the subpolar North Atlantic, which is largely driven by surface shortwave radiation increases, consistent with the forcing from AA reductions. Africa + Middle East AA reductions also involve excitation of a negative North Atlantic Oscillation pattern, which contributes to AMOC weakening. Our results show that efforts to improve air quality, particularly around the Atlantic basin but also far away in East Asia, will contribute to future AMOC weakening.

1. Introduction

The Atlantic Meridional Overturning Circulation (AMOC) represents the Atlantic branch of the global overturning circulation. It is a central component of the climate system, transporting heat, freshwater, carbon and nutrients (Buckley and Marshall 2016). By moving warm, salty water poleward and returning colder, denser water at depth, the AMOC shapes sea surface temperature (SST) patterns and modulates patterns of precipitation and storm tracks. Because it is sustained by a delicate balance of buoyancy forcing (surface heat loss and freshwater fluxes) and wind-driven circulation, the AMOC is sensitive to anthropogenic perturbations (Fox-Kemper *et al* 2021). Understanding how human activities affect the AMOC is therefore essential for projecting near- and long-term climate change, as well as associated risks to ecosystems and societies.

Increasing anthropogenic greenhouse gas (GHG) concentrations provide the dominant long-term push toward AMOC weakening (Gregory *et al* 2005, Cheng *et al* 2013, Weijer *et al* 2020). GHGs warm the surface, enhance upper-ocean stratification, and accelerate high-latitude hydrological cycle changes that increase freshwater input into the North Atlantic via precipitation, runoff and ice melt. These processes act to reduce surface water density and inhibit deep convection, which weakens the AMOC. The IPCC Sixth Assessment Report (AR6) assesses that the AMOC will very likely decline over the 21st century under all shared socioeconomic pathways (SSPs; Fox-Kemper *et al* 2021). This decline is relatively scenario-insensitive until mid-century, with stronger divergence as GHG emissions pathways separate (Weijer *et al* 2020). Multimodel end-of-century AMOC weakening ranges from 24% under SSP1-2.6 (a sustainability pathway leading to low GHGs) to 39% under SSP5-8.5 (a fossil fuel intensive pathway leading to high GHGs).

In contrast to GHGs, anthropogenic aerosols (AAs) through both direct radiative effects and aerosol-cloud interactions (Bellouin *et al* 2020) preferentially cool the Northern Hemisphere (Forster *et al* 2021). This increases North Atlantic surface ocean density via stronger ocean-to-atmosphere heat loss and reduced freshwater flux, thereby strengthening deep convection and opposing GHG-driven AMOC weakening (Delworth *et al* 2005, Delworth and Dixon 2006, Menary *et al* 2013, Hassan *et al* 2021, Robson *et al* 2022, Li *et al* 2023, Allen *et al* 2024). In Coupled Model Intercomparison Project version 6 (CMIP6; Eyring *et al* 2016) historical simulations, aerosol forcing is linked to multimodel mean AMOC strengthening of 10% over 1850–1985, and the model spread is related to a proxy for the strength of the aerosol forcing (Robson *et al* 2022). Moreover, this strengthening is larger than that simulated by CMIP5 simulations, which is consistent with the inclusion of aerosol-cloud interactions in more CMIP6 models (e.g. Booth *et al* 2012). However, AA forcing and/or the AMOC response may be overestimated in CMIP6 (Menary *et al* 2020, Hassan *et al* 2021, Robson *et al* 2022, Needham *et al* 2024, Li and Liu 2025).

AAs are also spatially heterogeneous and little is known about the impact of regional aerosol emissions on the AMOC. Liu *et al* (2024) recently conducted idealized experiments by decreasing solar insolation (a proxy for aerosol increases) by 10% (a very strong perturbation relative to typical anthropogenic changes) in the West (North America and Europe) and separately in the East (East Asia and South Asia). The West perturbation (reversed to mimic the post-1980s decrease in AA emissions there) yielded the anticipated AMOC weakening, consistent with the above studies focused on global aerosol perturbations (e.g. Hassan *et al* 2021). Perhaps surprisingly, the East perturbation (which mimics the increase in AA emissions there) also yielded AMOC weakening. This weakening was associated with a circumglobal teleconnection and a negative North Atlantic Oscillation (NAO)-like pattern, including weakened westerlies over subpolar North Atlantic, leading to a reduction in surface heat loss through changes in turbulent fluxes, and reduced deep water formation. Similar dynamical mechanisms are also highlighted in Diao *et al* (2021) and Li *et al* (2025). In particular, Li and Liu (2025) further support this pathway using idealized '10×sulfate' experiments within the Precipitation Driver and Response Model Intercomparison

(PDRMIP) project (Samset *et al* 2016). Thus, these idealized studies imply that the impact of AAs on the AMOC may depend on the location of the AA forcing, with opposite responses for East Asia and South Asia as compared to other regions.

Through the 21st century, both the magnitude and spatial distribution of aerosol forcing remains uncertain, with most future emissions scenarios yielding AA emissions decreases associated with efforts to improve air-quality (Lund *et al* 2019, Persad *et al* 2023, Samset *et al* 2024). As these efforts are pursued, they will unmask GHG driven warming (Allen *et al* 2020, 2021, Samet *et al* 2025), which may accelerate weakening of the AMOC (Ma *et al* 2020, Hassan *et al* 2022). For example, using four chemistry-climate models with experiments designed to target near-term climate forcer mitigation (ssp370 versus ssp370-lowNTCF), Hassan *et al* (2022) showed that reducing (global) aerosols and related precursors yields AMOC weakening on the order of ∼10% by end-of-the-century. The impact of future, regional decreases in AAs remains to be quantified, as do the mechanisms by which AA reductions in different regions affect the AMOC.

The Regional Aerosol Model Intercomparison Project (RAMIP) contains a comprehensive suite of simulations from CMIP6-era global climate models, specifically designed to improve our understanding of the climate effects associated with both global and regional aerosol reductions (Wilcox *et al* 2023). Here, we use eight RAMIP models (each with 10 ensemble members) to quantify the AMOC response to global aerosol reductions in line with realistic near-term policy choices, as well as regional aerosol reductions from four regions. Section 2 briefly summarizes the RAMIP experimental design and models, and also describes our methodologies. Section 3 presents results, including the AMOC response to global and regional AA reductions, the relationship to the aerosol effective radiative forcing (ERF), and the associated mechanisms. Conclusions and discussion follow in section 4.

2. Data and methods

2.1. Model experiments

2.1.1. Coupled ocean-atmosphere transient experiments

Following RAMIP (Wilcox *et al* 2023) protocols, we use pairs of transient (2015–2050) coupled ocean-atmosphere climate model simulations (supplementary table 1), initialized from the end of the CMIP6 historical simulations. The ScenarioMIP ssp370 simulation, which features weak levels of air quality control from the SSP3-7.0 scenario, is used as the baseline. All transient RAMIP simulations include prescribed concentrations of well-mixed GHGs and land use changes from SSP3-7.0. RAMIP perturbation experiments (e.g. ssp370-126aer) use an identical setup to ssp370 but take anthropogenic aerosol and precursor emissions of sulfur dioxide (SO_2), sulfate (SO_4), black carbon (BC), and organic aerosol (OA) from the SSP1-2.6 scenario, which features strong levels of air quality control. Perturbation experiments are conducted for the globe and four regions: Africa and Middle East; East Asia; North America and Europe; and South Asia. Each perturbation features ten ensemble members for each of the eight models (80 total simulations), which represents a balance between computational cost and additional information gained per ensemble member (Monerie *et al* 2022). The corresponding aerosol reduction signals are obtained by subtracting the baseline ssp370 experiment from each of the aerosol reduction experiments (e.g. ssp370-126aer-ssp370) on an annual basis. This yields a difference time series which is used to quantify the magnitude of the response.

2.1.2. Fixed SST (fSST) time slice experiments

To assess the aerosol ERF, we use pairs of RAMIP 30 year time-slice simulations, where SSTs, sea ice concentrations and land use are fixed to preindustrial monthly climatologies (supplementary table 2) (Pincus *et al* 2016, Wilcox *et al* 2023, Allen *et al* 2026). All time-slice simulations feature year 2050 GHGs, ozone and natural emissions from SSP3-7.0. The baseline experiment (piClim-370) also uses year 2050 anthropogenic aerosol and precursor gas emissions from SSP3-7.0. The global aerosol reduction experiment (i.e. piClim-370-126aer) is identical in all ways except it uses year 2050 anthropogenic aerosol and precursor gas emissions from SSP1-2.6. The regional aerosol reduction experiments (e.g. piClim-370-EAS126aer) also use year 2050 anthropogenic aerosol and precursor gas emissions from SSP1-2.6 within the region of consideration (e.g. East Asia) and SSP3-7.0 emissions otherwise. The corresponding aerosol reduction signals are obtained by subtracting the baseline piClim370 experiment from each of the aerosol reduction experiments (e.g. piClim370-126aer).

In both experimental setups, 'anthropogenic aerosol and precursor gas emissions' includes both industrial and biomass burning emissions of SO_2, SO_4, BC, and OA. However, the bulk of the emissions decrease is due to industrial (as opposed to biomass burning) emissions, e.g. 99% of the decrease in SO_2

Table 1. RAMIP models and their atmospheric resolution, aerosol scheme, RAMIP data reference and model reference.

Model	Atmos. Res.	Aerosol scheme	RAMIP data references	Model references
CanESM5-1	2.8° × 2.8°	Interactive (bulk)	Fraser-Leach *et al* (2025)	Swart *et al* (2019)
CESM2	0.9° × 1.25° 1.9° × 2.5° (piClim)	MAM4 (modal)	Allen (2025)	Danabasoglu *et al* (2020)
CNRM-ESM2-1	1.4° × 1.4°	TACTIC v2 (modal)	Nabat (2025)	Seferian *et al* (2019)
EC-Earth3-AerChem	0.7° × 0.7°	TM5 (modal)	O'Donnell *et al* (2025)	van Noije *et al* (2021)
MIROC6	1.4° × 1.4°	SPRINTARS 6.0 (bulk)	Takemura (2025)	Tatebe *et al* (2019)
MRI-ESM2-0	1.125° × 1.125°	MASINGAR mk2r4 (bulk)	Oshima and Koshiro (2025)	Yukimoto *et al* (2019)
NorESM2-LM	1.9° × 2.5°	OsloAero (modal)	Lewinschal (2025)	Seland *et al* (2020)
UKESM1-0-LL	1.25° × 1.875°	GLOMAP-mode (modal)	Rumbold *et al* (2025)	Sellar *et al* (2019)

emissions under the global perturbation is due to industrial emissions (Allen *et al* 2026). The seasonal cycle of emissions is included in all simulations. GLO refers to the global aerosol reduction signal; AFR refers to the Africa and Middle East aerosol reduction signal; EAS refers to the East Asia aerosol reduction signal; NAE refers to the North America and Europe aerosol reduction signal; and SAS refers to the South Asia aerosol reduction signal.

2.2. Models

Eight RAMIP models performed the transient and time slice simulations and archived the required variables for this analysis. Models include CanESM5-1, CESM2, CNRM-ESM2-1, EC-Earth3-AerChem, MIROC6, MRI-ESM2-0, NorESM2-LM, UKESM1-0-LL (table 1). All eight models include an interactive representation of aerosols (e.g. transport, removal). Seven models include a representation of both aerosol-cloud indirect effects. CNRM-ESM2-1 lacks the Albrecht (aerosol-cloud lifetime) effect. All model data is reinterpolated to a 2.5° × 2.5° grid. ERF analyses are based on all 30 years of the fSST experiments. Analyses based on the coupled ocean atmosphere transient simulations emphasize three 12 year time periods: 2015–2026; 2027–2038; and 2039–2050. In all cases, annual mean data is analyzed.

2.3. AMOC Definition

The AMOC is defined as the maximum annual mean stream function below 500 m at 28° N in the Atlantic Ocean, using the CMIP6 variables msftmz (ocean meridional overturning mass streamfunction) or msftyz (ocean Y overturning mass streamfunction). Similar AMOC changes are obtained with alternative AMOC definitions (e.g. at 40° N). AMOC units are Sverdrup (Sv), which is a unit for ocean current volume transport in 10^6 m^3 s^{-1}.

2.4. Surface density flux (SDF) definition

The SDF indicates the loss or gain of density (buoyancy) of the ocean surface due to thermal (radiation, sensible and latent heat) and saline (sea-ice melting/freezing, brine rejection, precipitation minus evaporation) exchanges (Liu *et al* 2017, 2019, Zhu and Liu 2025). An increase in subpolar North Atlantic SDF is associated with strengthening of the AMOC; a decrease in SDF is associated with weakening of the AMOC. SDF is defined as:

$$\mathrm{SDF} = -\alpha \frac{hfds}{c_p} - \rho(0, \mathrm{SST}) \times \beta \frac{wfo \times \mathrm{SSS}}{1 - \mathrm{SSS}} \tag{1}$$

where c_p, SST, and SSS are the specific heat capacity, SST, and salinity, respectively; α and β are thermal expansion and saline contraction coefficients; and $\rho(0, \mathrm{SST})$ is the density of freshwater with a salinity of zero and the temperature of SST. *hfds* represents the net surface heat flux into ocean (positive downward), which has contributions from shortwave (SW) and longwave (LW) radiation, sensible (SH) and latent (LH) heat fluxes, and heat fluxes from sea ice melting and other minor sources. *wfo* represents net surface freshwater flux into the ocean (positive downward) and has positive contributions from precipitation, runoff and ice melting and negative contributions from evaporation. The first term $-\alpha \frac{hfds}{c_p}$ represents the thermal contribution (TSDF); the second term $\rho(0, \mathrm{SST}) \times \beta \frac{wfo \times \mathrm{SSS}}{1 - \mathrm{SSS}}$ represents the saline contribution (SSDF) to the SDF. All SDF responses are reported in units of mg m^{-2} s^{-1}.

2.5. Other definitions

The North Atlantic is defined as the region from 20–70° N and 280–360° E. The subpolar North Atlantic, where most of the AMOC feedbacks occur, is defined as 50–65° N and 300–350° E (highlighted by green boxes in our figures).

Model agreement on the sign of the response is indicated when at least 6 of the 8 models agree. When this is not the case, the region is stippled. Uncertainty is quantified as the 90% confidence interval, estimated as $1.65 \times \frac{\sigma}{\sqrt{n}}$, where is the standard deviation across models and n is the number of models.

3. Results

3.1. North atlantic aerosol ERF and AOD

We first start with an analysis of the ERF (i.e. net change in top-of-the-atmosphere energy flux) from RAMIP fSST experiments, which represent the forced response. Coupled runs include feedbacks, which can be prominent for AMOC-related analyses (e.g. Hassan *et al* 2021, Robson *et al* 2022). Figure 1 shows the multimodel mean North Atlantic aerosol ERF from the fSST experiments, as well as the corresponding time series over the North Atlantic Ocean (20–70° N and 280–360° E). Note that fSST simulations are not transient, as AA emissions are held fixed at 2050 levels (based on SSP3-7.0 for the baseline experiment and SSP1-2.6 for the others), and thus provide an estimate of the aerosol forcing by the end of the coupled ocean atmosphere simulations. All experiments feature an increase in North Atlantic Ocean aerosol ERF (although not significant for SAS). GLO (figures 1(a) and (b)) yields the largest North Atlantic Ocean aerosol ERF at 1.08 ± 0.33 W m^{-2}, followed by NAE (figures 1(c) and (d)) at 0.61 ± 0.16 W m^{-2}; AFR (figures 1(e) and (f)) at W m^{-2}; EAS (figures 1(g) and (h)) at 0.10 ± 0.08 W m^{-2}; and SAS (figures 1(i) and (j)) at 0.04 ± 0.11 W m^{-2}. As will be shown below, these ERF values significantly correlate with the AMOC responses over the last 12 years (2039–2050) from the coupled runs, which supports the importance of local (i.e. North Atlantic) aerosol to the AMOC response. Most of the North America + Europe ERF occurs in the mid/high latitudes, whereas AFR yields its largest ERF in the subtropics. EAS and SAS yield weaker and more diffuse ERF, with less model agreement (especially for SAS), but ERF increases are in general largest south of Greenland/Iceland and west of the UK. For example, aerosol ERF over the subpolar North Atlantic (50–65° N and 300–350° E) Ocean increases to 0.18 ± 0.21 W m^{-2} for EAS and 0.10 ± 0.20 W m^{-2} for SAS, respectively. Qualitatively similar results are generally obtained for North Atlantic Ocean surface downwelling SW radiation and surface net SW radiation (although EAS yields slightly larger values than AFR). For the former, for example, GLO yields increases in North Atlantic Ocean downwelling surface SW radiation of 2.09 ± 0.58 W m^{-2}, followed by NAE at 0.92 ± 0.22 W m^{-2}; EAS at 0.34 ± 0.22 W m^{-2}; AFR at 0.31 ± 0.16 W m^{-2}; and SAS at W m^{-2}. Given the considerable distance EAS and SAS are from the North Atlantic, this shows the ability of atmospheric circulation to transport aerosols over large distances.

To more distinctly show the importance of North Atlantic aerosol, including the ability of long-range aerosol transport to this region (e.g. from EAS), supplementary figure 1 shows aerosol optical depth at 550 nm (AOD) responses from the coupled ocean-atmosphere simulations (which includes the temporal evolution of AA reductions). North Atlantic Ocean AOD begins to decrease early in the simulations (i.e. 2015–2026) and in general becomes progressively more negative. By the last 12 years (2039–2050), North Atlantic Ocean AOD significantly decreases in all simulations. GLO again yields the largest decrease at -13.6 ± 3.6 10^{-3}, followed by NAE at -5.3 ± 1.1 10^{-3}; AFR at -2.8 ± 0.6 10^{-3}; EAS at -2.3 ± 1.2 10^{-3}; and SAS at -1.4 ± 1.0 10^{-3}. Both EAS and SAS feature an increase in AOD near west Africa (with mixed model agreement), presumably due to dust feedbacks. Similar North Atlantic Ocean AOD decreases are obtained from the fSST experiments (years 1–30). Anthropogenic aerosols having a relatively short real-world atmospheric lifetime (due to wet and dry removal) of ∼4–7 d in the lower troposphere. This may be longer in some models, and it depends on the aerosol species (Textor *et al* 2006). UKESM1-0-LL, for example, has a SO_4 lifetime of 5.57 d (Mulcahy *et al* 2020), which is on the upper end of the range shown in AeroCom models of 3–5.4 d (Textor *et al* 2006). Nonetheless, RAMIP simulations suggest some aerosol is transported over relatively large distances (i.e. from EAS to the North Atlantic), likely due to lofting into the upper troposphere.

3.1.1. AMOC Response

Figure 2 shows the multimodel mean Atlantic depth-latitude meridional stream function responses for three time periods (2015–2026; 2027–2038; and 2039–2050) and the corresponding AMOC (maximum stream function below 500 m at 28° N in the Atlantic Ocean) time series for each of the aerosol

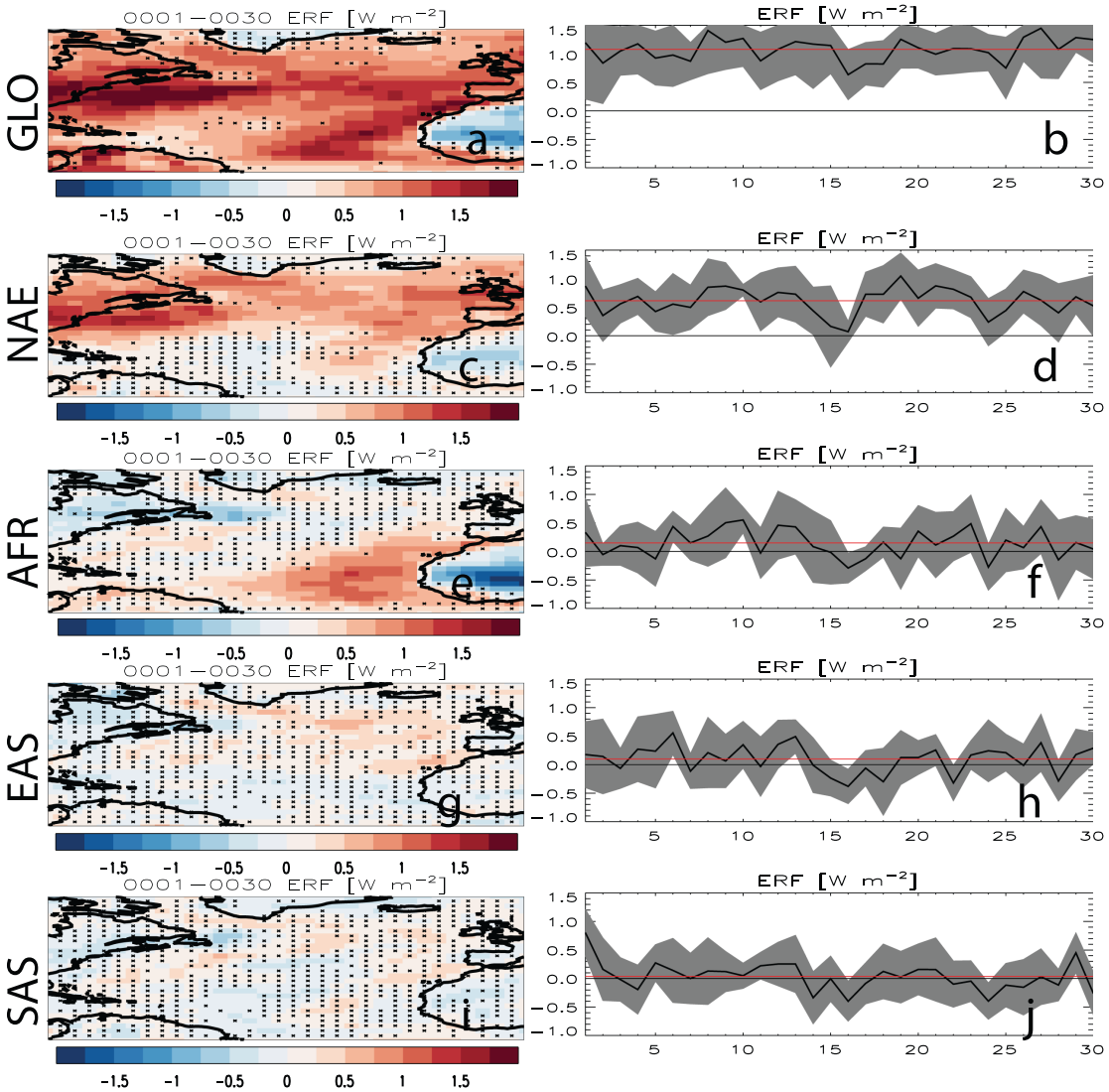

Figure 1. Multimodel mean North Atlantic aerosol ERF and North Atlantic Ocean ERF time series from fixed SST experiments. Panels show responses for (a) and (b) Global; (c) and (d) North America + Europe; (e) and (f) Africa + Middle East; (f) and (h) East Asia; and (i) and (j) South Asia aerosol reductions. Non-stippled regions indicate at least 6 of the 8 models agree on the sign of the response. North Atlantic Ocean ERF time series (b, d, f, h, j) includes the uncertainty (gray shading) estimated as the 90% confidence interval across models, as well as the multimodel mean (red line). ERF comes from 30 year fixed SST experiments with aerosol and precursor gas emissions reductions from the year 2050. Units are W m^{-2}.

reduction perturbations. As defined above, aerosol reduction signals are obtained by subtracting the baseline ssp370 experiment from each of the aerosol reduction experiments (e.g. ssp370-126aer) on an annual basis. This yields a difference time series which is used to quantify the magnitude of the response, i.e. the 2015–2026 response compares the baseline ssp370 experiment with an aerosol reduction experiment over the first 12 years; the 2027–2038 response compares the baseline ssp370 experiment with an aerosol reduction experiment over the middle 12 years; and the 2039–2050 response compares the baseline ssp370 experiment with an aerosol reduction experiment over the final 12 years. In general, the stream function continues to decrease in strength as one progresses through the three time periods (consistent with AOD; supplementary figure 1), with maximum weakening near the climatological maximum stream function (around 30–40° N at 1000 m depth). Model agreement (lack of stippling) on this decrease also tends to improve as time progresses. These statements are particularly true for GLO, NAE and AFR. GLO shows acceleration of AMOC weakening from -0.16 ± 0.15 Sv for 2015–2026 to -0.45 ± 0.23 Sv for 2027–2038 and to -0.98 ± 0.40 Sv for 2039–2050. Similarly, NAE AMOC weakening for the three consecutive time periods accelerates from -0.02 ± 0.04 Sv to Sv and to -0.34 ± 0.18 Sv, respectively. AFR AMOC weakening also accelerates from -0.05 ± 0.05 Sv

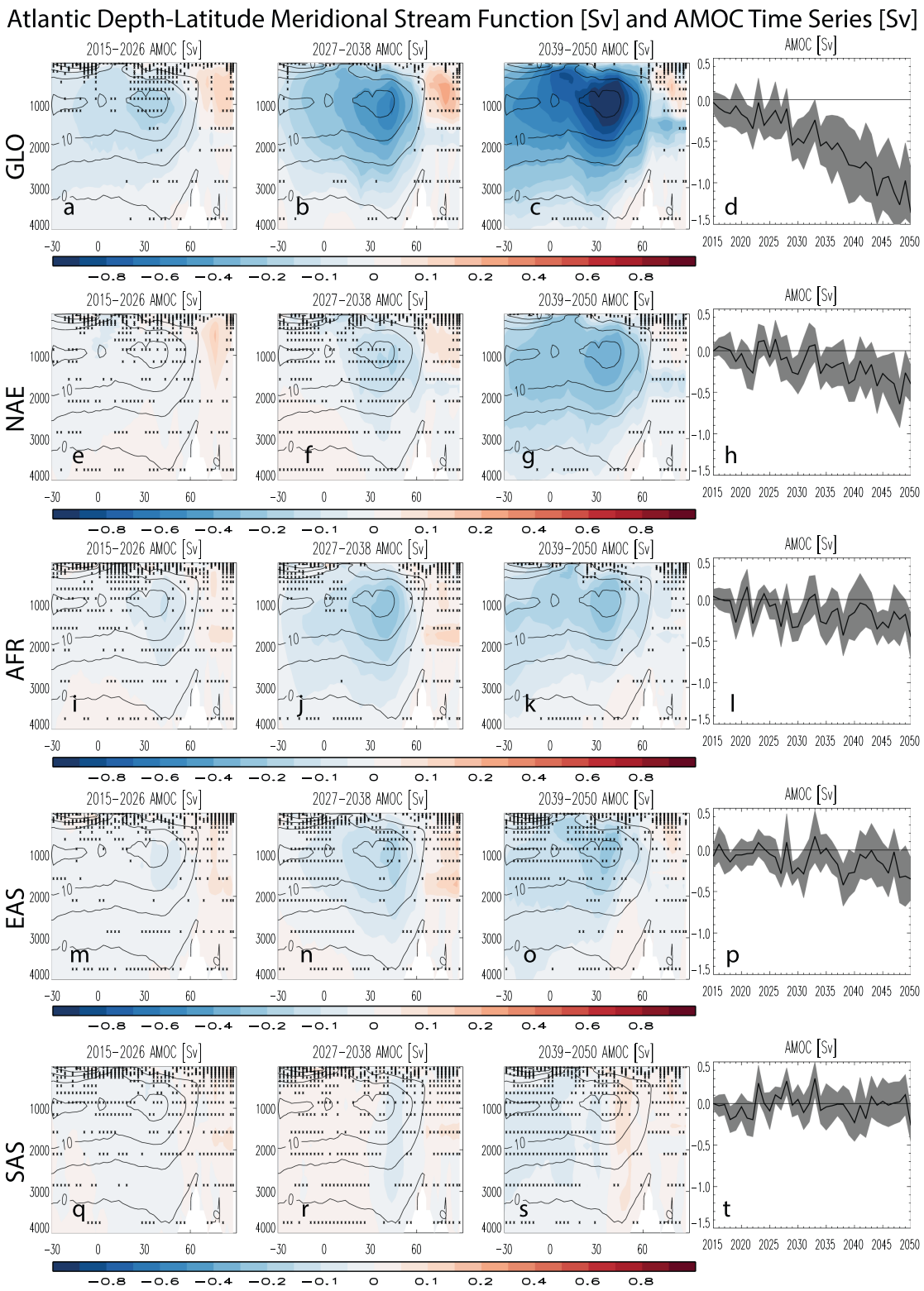

Figure 2. Multimodel mean Atlantic depth-latitude meridional steam function responses and AMOC time series. Panels show responses for (a)–(d) Global; (e)–(h) North America + Europe; (i)–(l) Africa + Middle East; (m)–(p) East Asia; and (q)–(t) South Asia aerosol reductions. Atlantic depth-latitude meridional steam function responses are shown for three 12 year time periods including (a, e, i, m, q) 2015–2026; (b, f, j, n, r) 2027–2038; and (c, g, k, o, s) 2039–2050. Non-stippled regions indicate at least 6 of the 8 models agree on the sign of the response. Climatological stream function (based on the first time period from 2015–2026 from the baseline ssp370 experiment) is shown as a thin black line in all cross-section panels. AMOC time series includes the uncertainty (gray shading), estimated as the 90% confidence interval across models. Units are Sv.

to -0.19 ± 0.09 Sv and to -0.22 ± 0.14 Sv. Although there is less model agreement, EAS AMOC weakening accelerates from -0.04 ± 0.06 Sv for 2015–2026 to -0.13 ± 0.14 Sv for 2027–2038 and to -0.19 ± 0.18 Sv for 2039–2050. SAS yields AMOC weakening of -0.04 ± 0.04 Sv for 2015–2026, nonsignificant AMOC strengthening of 0.03 ± 0.07 Sv for 2027–2038, and non-significant weakening of Sv for 2039–2050. supplementary figure 2 shows a similar (but stronger) AMOC response under the baseline ssp370 experiment (which features large GHG increases), with 2039–2050 AMOC weakening of -3.0 ± 0.78 Sv.

Supplementary figure 3 shows corresponding plots for the annual mean ocean mixed layer depth (MLD), which exhibits subpolar North Atlantic evolution similar to the AMOC, consistent with weakened convection and reduced deep water formation (Liu and Liu 2013). By 2039–2050, the multimodal mean subpolar North Atlantic MLD decreases in all perturbations (not significant for SAS) at -17.5 ± 8.8 m for GLO; -6.2 ± 3.8 m for NAE; -5.2 ± 4.4 m for EAS; -4.9 ± 2.9 m for AFR; and -1.6 ± 2.0 m for SAS. The corresponding linear correlation (r) with the AMOC responses (across experiments) is 1.0. Thus, perturbations that feature larger decreases in MLD also feature larger AMOC weakening. Furthermore, the correlation between the AMOC and MLD responses across models is significant at the 90% confidence level for each experiment (outside of SAS) at $r = 0.90$ for GLO; 0.99 for NAE; 0.88 for EAS; 0.74 for AFR; and 0.64 for SAS. Thus, models that yield larger decreases in MLD also yield larger AMOC weakening.

Figure 3 emphasizes AMOC responses over the last 12 years of the experiments (2039–2050) for each model and each experiment, as well as the multimodel mean (MMM; black). As mentioned above, GLO (figure 3(a)) yields the largest multimodel mean AMOC weakening of Sv, and all 8 models yield a decrease. This weakening is about 1/3 as large as the corresponding weakening under the baseline ssp370 experiment (which features large GHG increases) at -3.0 ± 0.78 Sv with all 8 models yielding a decrease. The intermodel AMOC spread under GLO is relatively large with NorESM2-LM yielding AMOC weakening of -1.97 ± 0.32 Sv versus CNRM-ESM2-1 at -0.10 ± 0.20 Sv. NAE (figure 3(b)) yields the second largest multimodel mean AMOC weakening at -0.34 ± 0.18 Sv, and 7 of the 8 models yield a decrease. Similar to GLO, NorESM2-LM yields the strongest NAE AMOC weakening at -0.94 ± 0.24 Sv and CNRM-ESM2-1 is the lone model that yields a nonsignificant response. AFR (figure 3(c)) yields the next largest multimodel mean AMOC weakening at -0.22 ± 0.14 Sv with 7 of the 8 models yielding a decrease. NorESM2-LM again yields the strongest weakening for AFR at Sv. EAS (figure 3(d)) yields the next largest multimodel mean AMOC weakening at -0.19 ± 0.18 Sv with 5 of the 8 models yielding a decrease. As with the above perturbations, NorESM2-LM yields the strongest AMOC weakening for EAS at -0.82 ± 0.39 Sv. Three models, including MRI-ESM2-0, UKESM1-0-LL and CNRM-ESM2-1 yield a nonsignificant response. SAS (figure 3(e)) yields non-significant multimodel mean AMOC weakening at -0.05 ± 0.13 Sv with 5 of the 8 models yielding a decrease. NorESM2-LM continues to yield the strongest AMOC weakening at -0.46 ± 0.35 Sv. Only MRI-ESM2-0 yields significant AMOC strengthening at 0.29 ± 0.21 Sv. We therefore do not find robust evidence for an opposite AMOC response to East Asia or South Asia AA emissions reductions compared to reductions over North America and Europe (as in Liu *et al* 2024).

Figure 4 shows that the multimodel mean AMOC response (2039–2050) across experiments is consistent with the North Atlantic Ocean aerosol ERF (from fSST simulations), as the linear correlation is -0.95, significant at the 99% confidence level. The ERF from fSST runs is used here to relate the magnitude of the AMOC response across RAMIP perturbations to a quantity that represents the forced response (the coupled runs will include feedbacks, which can be prominent for AMOC-related analyses). Aerosol perturbations that feature larger positive ERF (e.g. GLO; NAE; and AFR) are associated with larger AMOC weakening. Similar results are obtained if surface downwelling SW radiation or net surface SW radiation are used, with correlations of -0.95. Furthermore, a similar (but positive) correlation is obtained if we use North Atlantic Ocean AOD from the coupled simulations, where $r = 1.0$ (figure 4(b)). The corresponding correlation based on net TOA energy flux from the coupled simulations is also significant ($r = -0.90$; significant at the 95% confidence level). We note that there are only five points in these correlations, which are also heavily influenced by the relatively large GLO responses. All of these results support the importance of North Atlantic aerosol to the AMOC response.

Consistent with prior work (e.g. Weijer *et al* 2020), figure 5 shows that the intermodel spread in the AMOC response (2039–2050) for a given experiment is generally related to each model's AMOC climatology. Here, the climatology is based on year 2015 (as opposed to 2015–2026) from the baseline ssp370 experiment using all realizations (effectively providing 10 years of 2015 climatology). This is to avoid biasing the climatology, since 2015–2026 includes some weakening. We also lack historical data for all ensemble members, which precludes a 12 year present-day climatology. Each experiment yields a negative correlation, which ranges from for GLO (figure 5(a)) to -0.27 for SAS (figure 5(e)). AFR

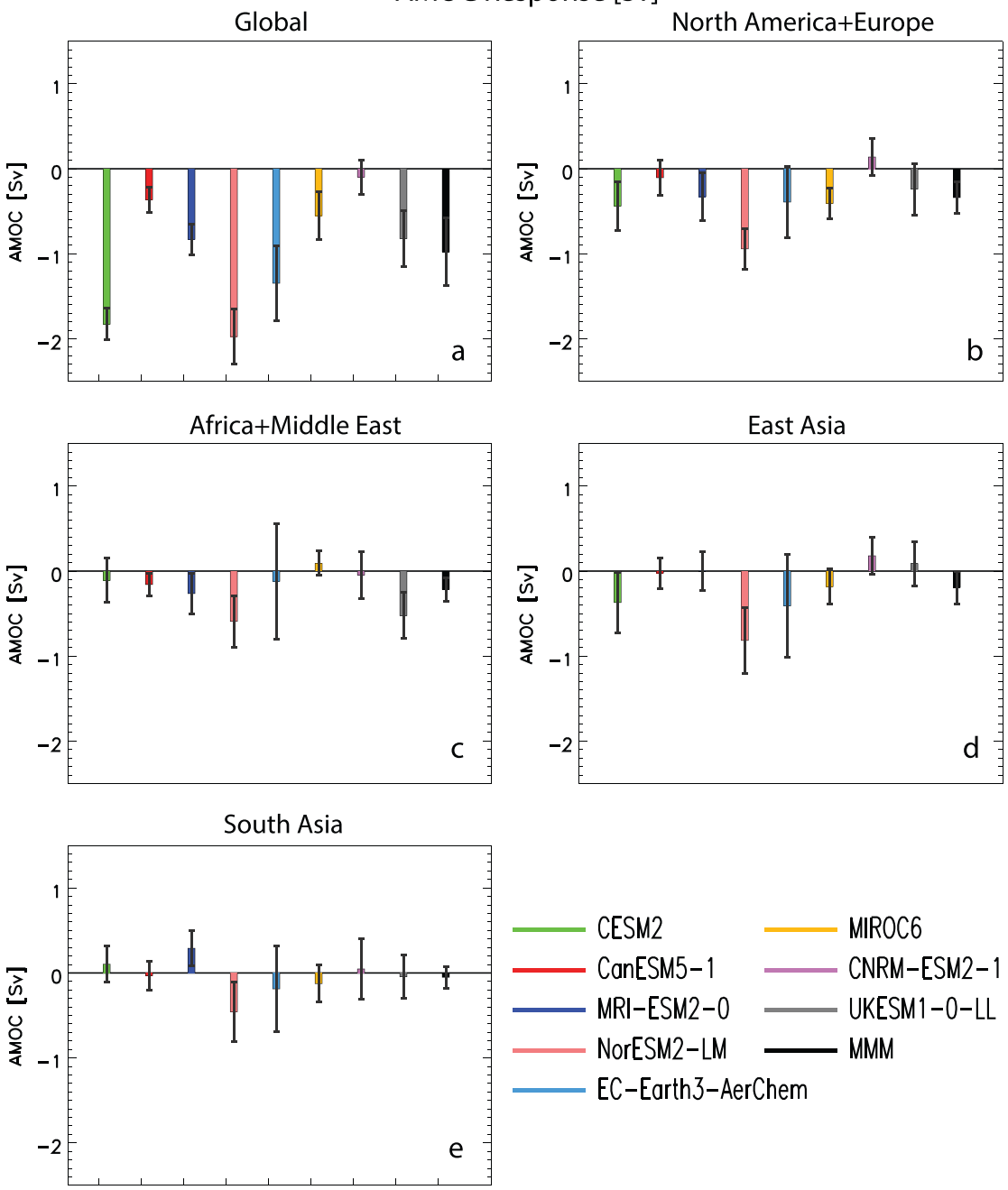

Figure 3. AMOC response to AA reductions. AMOC response (Sv) over the last 12 years of the simulation (2039–2050) for (a) Global; (b) North America + Europe; (c) Africa + Middle East; (d) East Asia; and (e) South Asia aerosol reductions. Colored bars show model mean responses for each of the eight models, including the uncertainty estimated as the 90% confidence interval. The multimodel mean response is shown as the black bar.

(figure 5(c)) and SAS (figure 5(e)) are not significant at the 90% confidence level. Thus, models with a stronger climatological AMOC tend to have larger AMOC weakening. The intermodel AMOC spread is less well explained by the intermodel North Atlantic Ocean ERF. Although these correlations are negative (as expected) and significant at the 95% confidence level for GLO and NAE ($r = -0.73$ and, respectively), they are weak and not significant for AFR ($r = 0.03$), EAS ($r = -0.07$) and SAS ($r = 0.12$).

3.2. AMOC mechanisms

Figures 6–10 show multimodal mean annual mean maps (for the three time periods) and subpolar North Atlantic time series for several quantities related to the AMOC, for GLO (figure 6) and each regional perturbation (figures 7–10). The top two rows of each figure show (SST; panels (a)–(d)) and sea surface salinity (SSS; panels (e)–(h)) responses. For the AA perturbations that yield significant AMOC weakening (all except SAS; figure 10), subpolar North Atlantic SST increases through the first two time

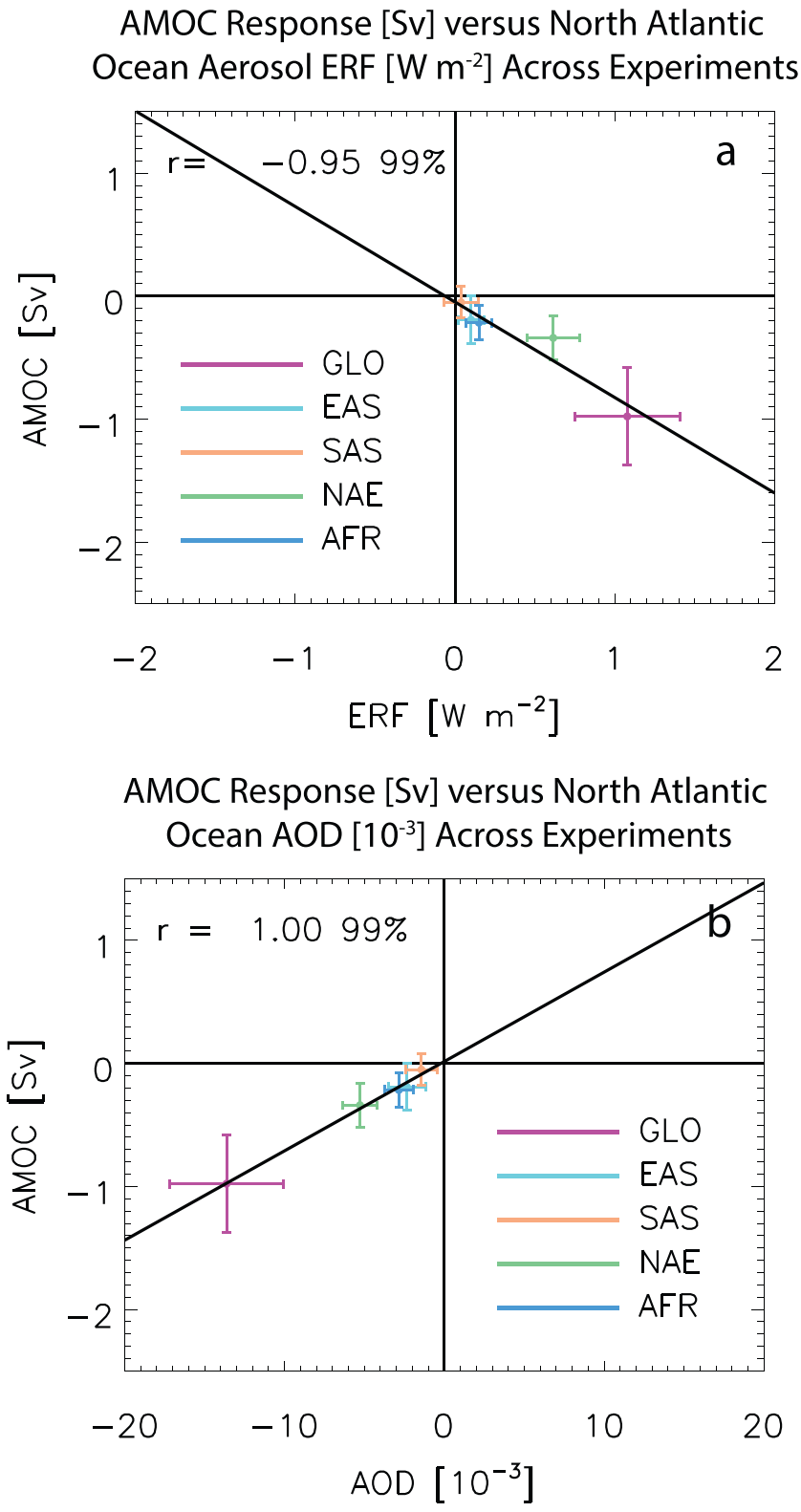

Figure 4. AMOC response versus aerosol metrics. Multimodel mean AMOC response (Sv) over the last 12 years of the simulation (2039–2050) versus multimodel mean North Atlantic Ocean (a) aerosol ERF (W m^{-2}) from fSST simulations and (b) aerosol optical depth (AOD) from coupled simulations. Each colored symbol represents the multimodel mean from one of the five aerosol reduction experiments. Uncertainty is estimated as the 90% confidence interval. Also included is the linear regression line (black), the correlation coefficient (r) and its significance level (e.g. 90%, 95% or 99%).

periods (2015–2026 and 2027–2038) with maximum warming during 2027–2038, followed by muted warming/cooling (especially south of Greenland/Iceland) during the final 12 years (2039–2050). This behavior is consistent with AA reductions driving warming, which reduces sea surface density and initiates AMOC weakening. This is followed by a **negative** AMOC feedback whereby less heat is transported

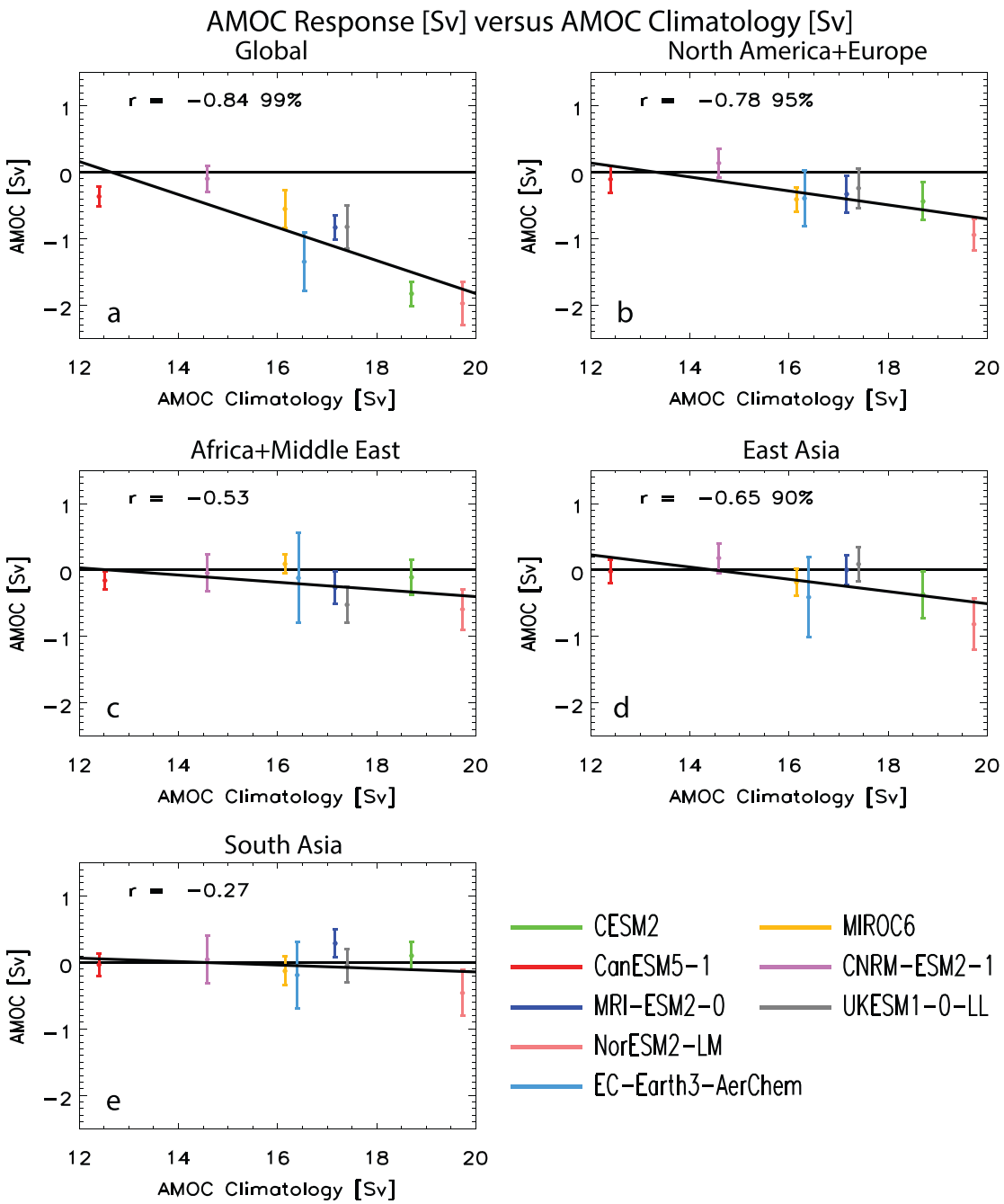

Figure 5. AMOC response versus AMOC climatology. AMOC response (Sv) over the last 12 years of the simulation (2039–2050) versus AMOC climatology based on the first year of the baseline ssp370 simulation (2015) for (a) Global; (b) North America + Europe; (c) Africa + Middle East; (d) East Asia; and (e) South Asia aerosol reductions. Colored lines show model mean values for each of the eight models, including the AMOC response uncertainty estimated as the 90% confidence interval. Also included is the linear regression line (black), correlation coefficient (r) and its significance level (e.g. 90%, 95% or 99%).

poleward (Liu *et al* 2020), muting the AA forced warming (Ma *et al* 2020, Hassan *et al* 2021, 2022, Allen *et al* 2024) as well as the decrease in sea surface density. Compared to the subpolar North Atlantic SST response, the SSS response is delayed, with minimal changes through 2015–2026, and also 2027–2038 in most perturbations (GLO is the exception). By 2039–2050, however, maximum decreases in subpolar North Atlantic SSS occur. This behavior is consistent with a delayed positive AMOC feedback whereby less salt is transported poleward under AMOC weakening, which acts to reduce sea surface density and maintain AMOC weakening. Thus, initial AMOC weakening is consistent with subpolar North Atlantic SST warming (a consequence of the AA reductions), which is subsequently buttressed by the AMOC-salt advection feedback (Stommel 1961, Rahmstorf 1996).

This is further supported by investigation of the subpolar North Atlantic (SDF; **panels i-l**), which indicates the loss or gain of density (buoyancy) of the ocean surface due to thermal and saline exchanges

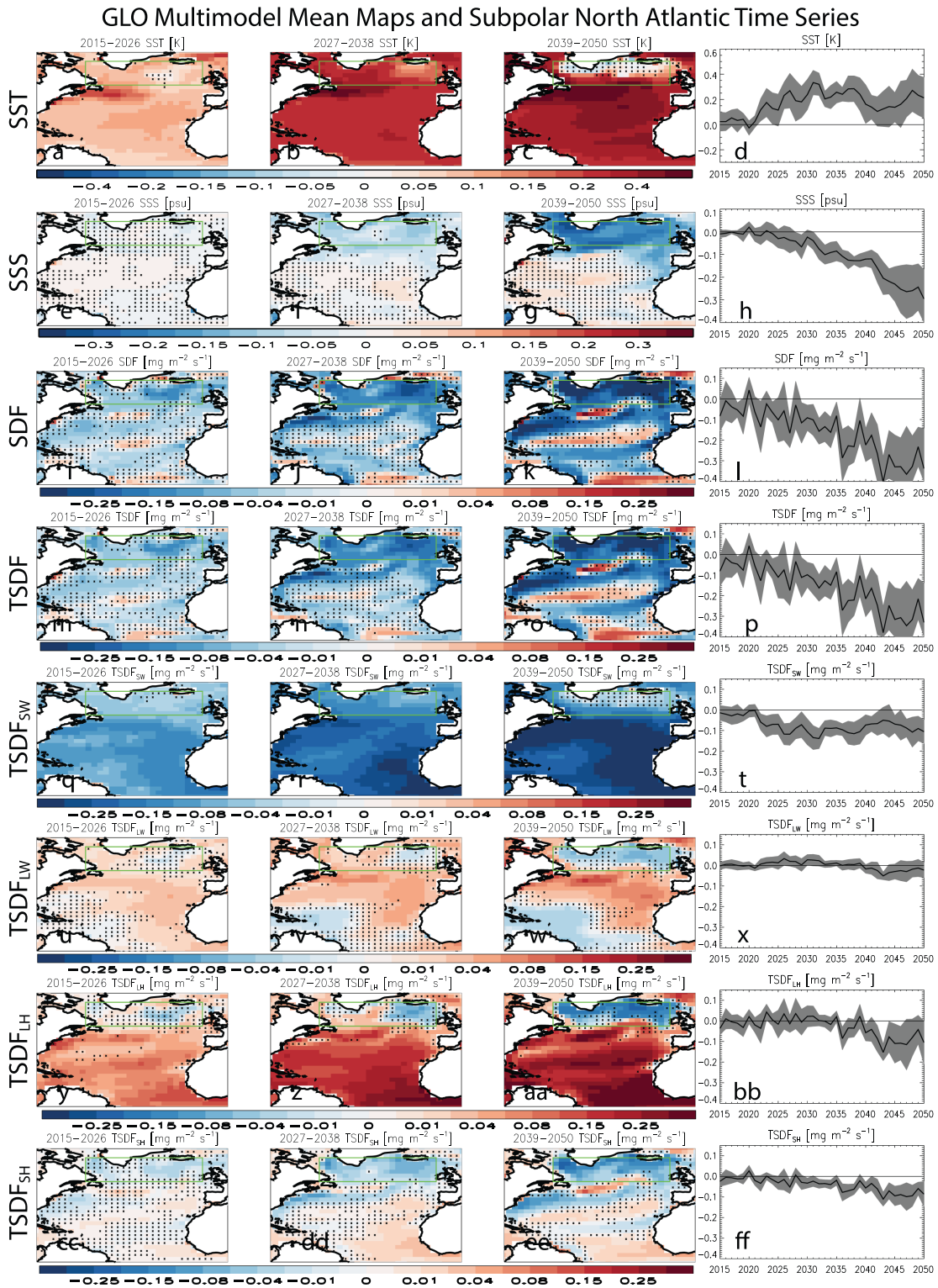

Figure 6. GLO multimodel mean maps and subpolar North Atlantic time series. Panels show responses for (a)–(d) sea surface temperature (K); (e)–(h) sea surface salinity (psu); (i)–(l) surface density flux (mg m^{-2} s^{-1}); (m)–(p) thermal component of SDF (mg m^{-2} s^{-1}); (q)–(t) shortwave radiation component of TSDF (mg m^{-2} s^{-1}); (u)–(x) longwave radiation component of TSDF (mg m^{-2} s^{-1}); (y)–(bb) latent heat component of TSDF (mg m^{-2} s^{-1}); and (cc)–(ff) sensible heat component of TSDF (mg m^{-2} s^{-1}). Responses are shown for three 12 year time periods including (a, e, i, m, q, u, y, cc) 2015–2026; (b, f, j, n, r, v, z, dd) 2027–2038; and (c, g, k, o, s, w, aa, ee) 2039–2050. Non-stippled regions indicate at least 6 of the 8 models agree on the sign of the response. Subpolar North Atlantic (green box) time series includes the uncertainty (gray shading), estimated as the 90% confidence interval across models.

(Liu *et al* 2017, 2019). For each AA perturbation, SDF evolution closely corresponds to the AMOC. By 2039–2050, the multimodel mean subpolar North Atlantic SDF decreases in all perturbations (not significant for SAS) at -0.28 ± 0.11 mgm^{-2} s^{-1} for GLO; -0.08 ± 0.05 mg m^{-2} s^{-1} for NAE; $-0.06 \pm$

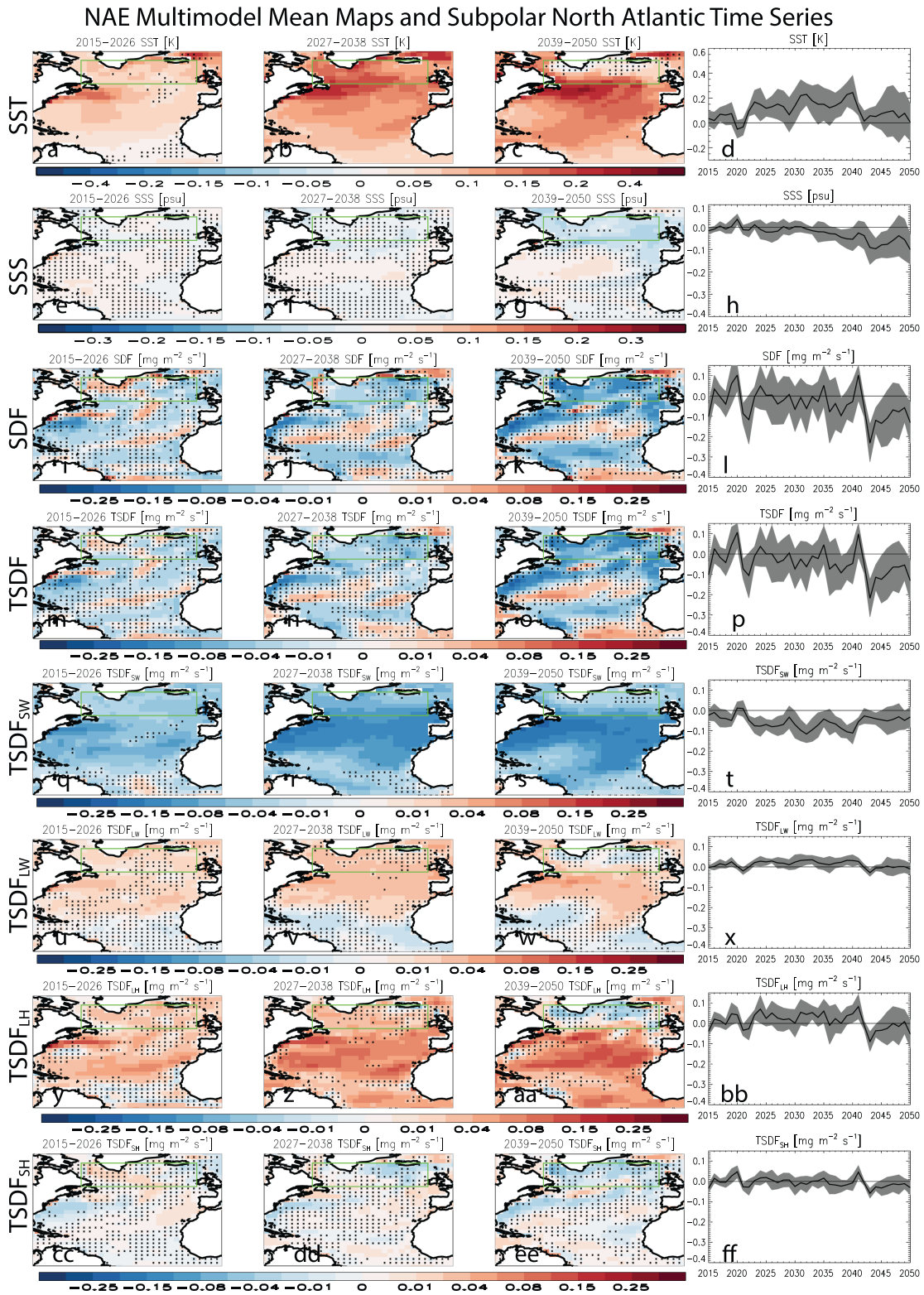

Figure 7. NAE multimodel mean maps and subpolar North Atlantic time series. Panels show responses for (a)–(d) sea surface temperature (K); (e)–(h) sea surface salinity (psu); (i)–(l) surface density flux (mg m^{-2} s^{-1}); (m)–(p) thermal component of SDF (mg m^{-2} s^{-1}); (q)–(t) shortwave radiation component of TSDF (mg m^{-2} s^{-1}); (u)–(x) longwave radiation component of TSDF (mg m^{-2} s^{-1}); (y)–(bb) latent heat component of TSDF (mg m^{-2} s^{-1}); and (cc)–(ff) sensible heat component of TSDF (mg m^{-2} s^{-1}). Responses are shown for three 12 year time periods including (a, e, i, m, q, u, y, cc) 2015–2026; (b, f, j, n, r, v, z, dd) 2027–2038; and (c, g, k, o, s, w, aa, ee) 2039–2050. Non-stippled regions indicate at least 6 of the 8 models agree on the sign of the response. Subpolar North Atlantic (green box) time series includes the uncertainty (gray shading), estimated as the 90% confidence interval across models.

0.04 mg m^{-2} s^{-1} for AFR; -0.05 ± 0.05 mg m^{-2} s^{-1} for EAS; and -0.01 ± 0.04 mg m^{-2} s^{-1} for SAS. The corresponding linear correlation with the AMOC responses (across experiments) is 1.0. Thus, perturbations that feature larger SDF decreases also feature larger AMOC weakening. Furthermore, the correlation between the AMOC and SDF responses across models is significant at the 90% confidence level for each experiment at $r = 0.95$ for GLO; 0.83 for NAE; 0.95 for AFR; 0.96 for EAS; and 0.73 for SAS. Thus, models that yield larger decreases in SDF also yield larger AMOC weakening.

Nearly all of the decrease in subpolar North Atlantic SDF is related to its thermal component (TSDF; **panels m–p**) (Hassan *et al* 2021, Robson *et al* 2022, Allen *et al* 2024, Lai *et al* 2025). The saline contribution (SSDF) is also negative but much weaker (supplementary figure 4). For example, the subpolar North Atlantic SSDF response under GLO for the last 12 years (2039–2050) is -0.015 ± 0.006 mg m^{-2} s^{-1}. The corresponding decrease in TSDF is more than an order of magnitude larger at -0.27 ± 0.11 mg m^{-2} s^{-1}. Similar conclusions apply for the regional aerosol perturbations. In the context of Arctic sea ice melt, it takes decade(s) for sea-ice induced freshwater to spread to the subpolar North Atlantic (Liu *et al* 2019, Liu and Federov, 2022). This implies changes in precipitation, evaporation, runoff and sea ice melt lead to relatively small decreases in SSDF (and in turn, SDF).

Further decomposing TSDF into its respective components shows that SW radiation ($TSDF_{SW}$; **panels q–t**) initiates the decrease in TSDF (see also supplementary figure 5), with maximum $TSDF_{SW}$ reductions during the first (2015–2026) and second time period (2027–2038). The other components of TSDF, including LW radiation ($TSDF_{LW}$; **panels u–x**), latent heat flux ($TSDF_{LH}$; **panels y–bb**) and sensible heat flux ($TSDF_{SH}$; **panels cc–ff**), exhibit weak changes (which in some cases are positive; supplementary figure 5) during the first two time periods, but maximum reductions occur during the latter time period (2039–2050). These results are consistent with the importance of the AA reductions driving enhanced subpolar North Atlantic SW radiation and reduced $TSDF_{SW}$ (and SDF) in the earlier time periods. For example, based on GLO, subpolar North Atlantic net SW radiation significantly increases in the first (2015–2026) and second (2027–2038) time periods at 0.56 ± 0.22 W m^{-2} and 1.12 ± 0.56 W m^{-2}, respectively (supplementary figure 6). As mentioned above, this initiates AMOC weakening and subsequently leads to subpolar North Atlantic SST cooling via reduced poleward heat transport. This cooling in turn drives reductions in upwards surface LW radiation (increases in net LW) and increases in downwards surface turbulent heat fluxes. Based on GLO, subpolar North Atlantic net LW radiation, as well as downwards LH and SH, become progressively more positive, with maximum increases in the last (2039–2050) time period of 0.73 ± 0.42 W m^{-2}, 2.2 ± 1.2 W m^{-2} and 2.0 ± 0.81 W m^{-2}, respectively (Supplementary figure 6). These in turn result in decreased $TSDF_{LW}$, $TSDF_{LH}$ and $TSDF_{SH}$, which help to maintain the overall decrease in SDF and in turn, AMOC weakening.

The response to Africa + Middle East AA reductions (figure 8) shows a tripolar North Atlantic SST pattern that peaks during 2027–2038 (figure 8(b)), including warming in the subtropics, cooling in the midlatitudes, and warming in the subpolar North Atlantic. Such a pattern has been related to the negative phase of the NAO, which is associated with weakening of the Azores high pressure and Icelandic low pressure, which in turn weakens the subpolar North Atlantic surface winds (Deser *et al* 2010). Supplementary figure 7 shows that these responses exist and are stronger in the four models that yield significant AMOC weakening for AFR (CanESM5-1, MRI-ESM2-0, NorESM2-LM, UKESM1-0-LL) as compared to the other four models that do not (CESM2, EC-Earth3-AerChem, MIROC6, CNRM-ESM2-1). For the former four models, sea level pressure decreases in the southern North Atlantic (15–50° N; 300–350° E) by -0.12 ± 0.05 hPa and increases in the northern North Atlantic (55–80° N; 300–350° E) by 0.29 ± 0.13 hPa, yielding a decrease in the meridional pressure gradient (southern minus northern North Atlantic) of -0.41 ± 0.16 hPa. A corresponding decrease in subpolar North Atlantic surface wind speeds also occurs at -0.06 ± 0.03 m s^{-1}. Weaker (and not significant) responses occur in the latter four models (those that do not yield significant AMOC weakening). Thus, AMOC weakening under AFR (in CanESM5-1, MRI-ESM2-0, NorESM2-LM, UKESM1-0-LL) appears to be related to a negative NAO-like response, which weakens subpolar North Atlantic winds and reduces turbulent heat loss from the ocean (supplementary figure 8 shows larger 2027–2038 $TSDF_{LH}$ and $TSDF_{SH}$ decreases in the four models with significant AMOC weakening versus the other four models), resulting in subpolar North Atlantic warming and reduced sea surface density. Outside of GLO (also during 2027–2038), the other AA perturbations do not yield a negative NAO-like response (supplementary figure 9). This lack of a NAO-like response includes EAS and SAS, which is dissimilar from that found in Liu *et al* (2024). There, a negative NAO-like response occurred in response to an increase in Asian anthropogenic aerosols, which weakened surface winds and heat fluxes in the subpolar North Atlantic.

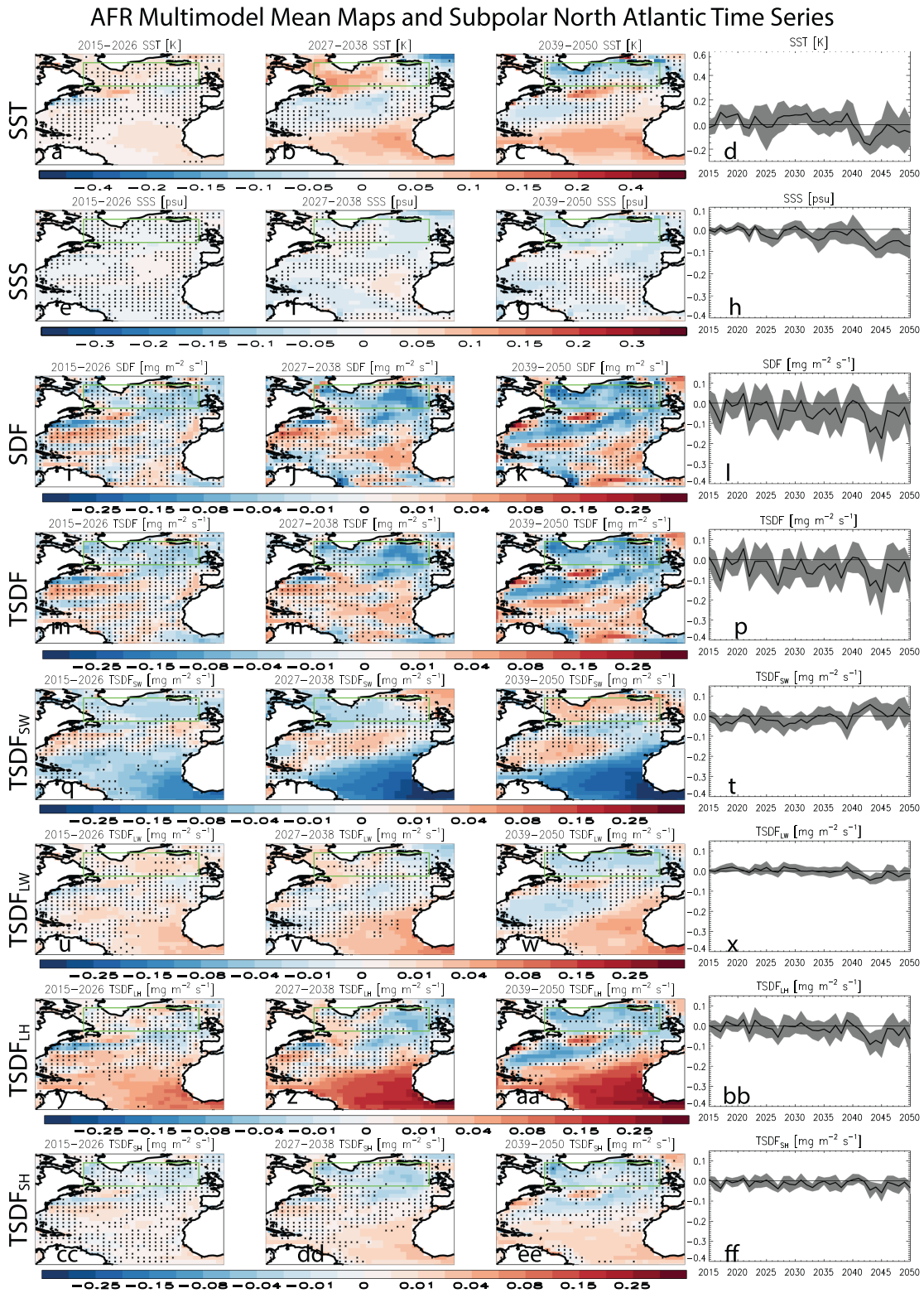

Figure 8. AFR multimodel mean maps and subpolar North Atlantic time series. Panels show responses for (a)–(d) sea surface temperature (K); (e)–(h) sea surface salinity (psu); (i)–(l) surface density flux (mg m^{-2} s^{-1}); (m)–(p) thermal component of SDF (mg m^{-2} s^{-1}); (q)–(t) shortwave radiation component of TSDF (mg m^{-2} s^{-1}); (u)–(x) longwave radiation component of TSDF (mg m^{-2} s^{-1}); (y)–(bb) latent heat component of TSDF (mg m^{-2} s^{-1}); and (cc)–(ff) sensible heat component of TSDF (mg m^{-2} s^{-1}). Responses are shown for three 12 year time periods including (a, e, i, m, q, u, y, cc) 2015–2026; (b, f, j, n, r, v, z, dd) 2027–2038; and (c, g, k, o, s, w, aa, ee) 2039–2050. Non-stippled regions indicate at least 6 of the 8 models agree on the sign of the response. Subpolar North Atlantic (green box) time series includes the uncertainty (gray shading), estimated as the 90% confidence interval across models.

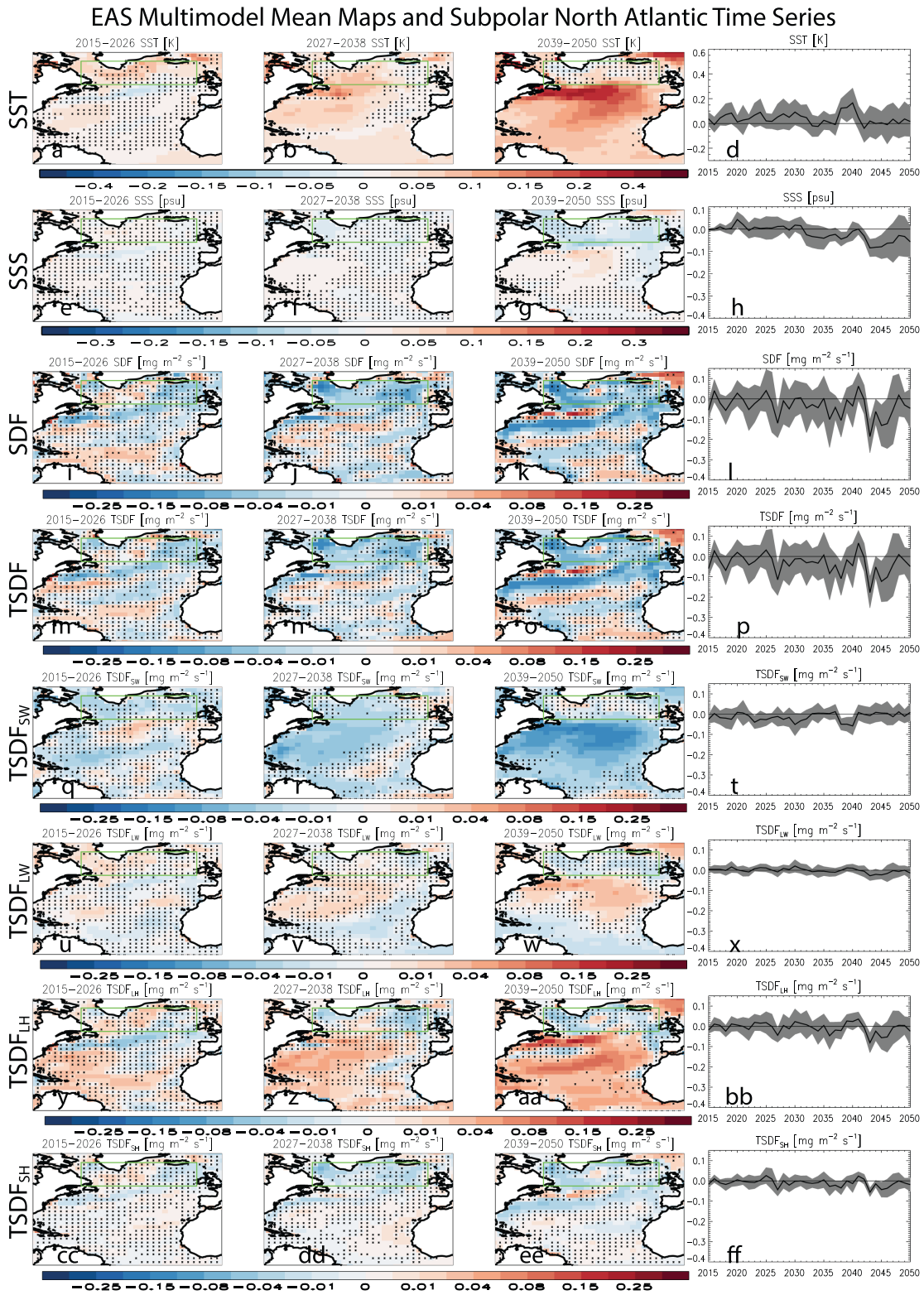

Figure 9. EAS multimodel mean maps and subpolar North Atlantic time series. Panels show responses for (a)–(d) sea surface temperature (K); (e)–(h) sea surface salinity (psu); (i)–(l) surface density flux (mg m^{-2} s^{-1}); (m)–(p) thermal component of SDF (mg m^{-2} s^{-1}); (q)–(t) shortwave radiation component of TSDF (mg m^{-2} s^{-1}); (u)–(x) longwave radiation component of TSDF (mg m^{-2} s^{-1}); (y)–(bb) latent heat component of TSDF (mg m^{-2} s^{-1}); and (cc)–(ff) sensible heat component of TSDF (mg m^{-2} s^{-1}). Responses are shown for three 12 year time periods including (a, e, i, m, q, u, y, cc) 2015–2026; (b, f, j, n, r, v, z, dd) 2027–2038; and (c, g, k, o, s, w, aa, ee) 2039–2050. Non-stippled regions indicate at least 6 of the 8 models agree on the sign of the response. Subpolar North Atlantic (green box) time series includes the uncertainty (gray shading), estimated as the 90% confidence interval across models.

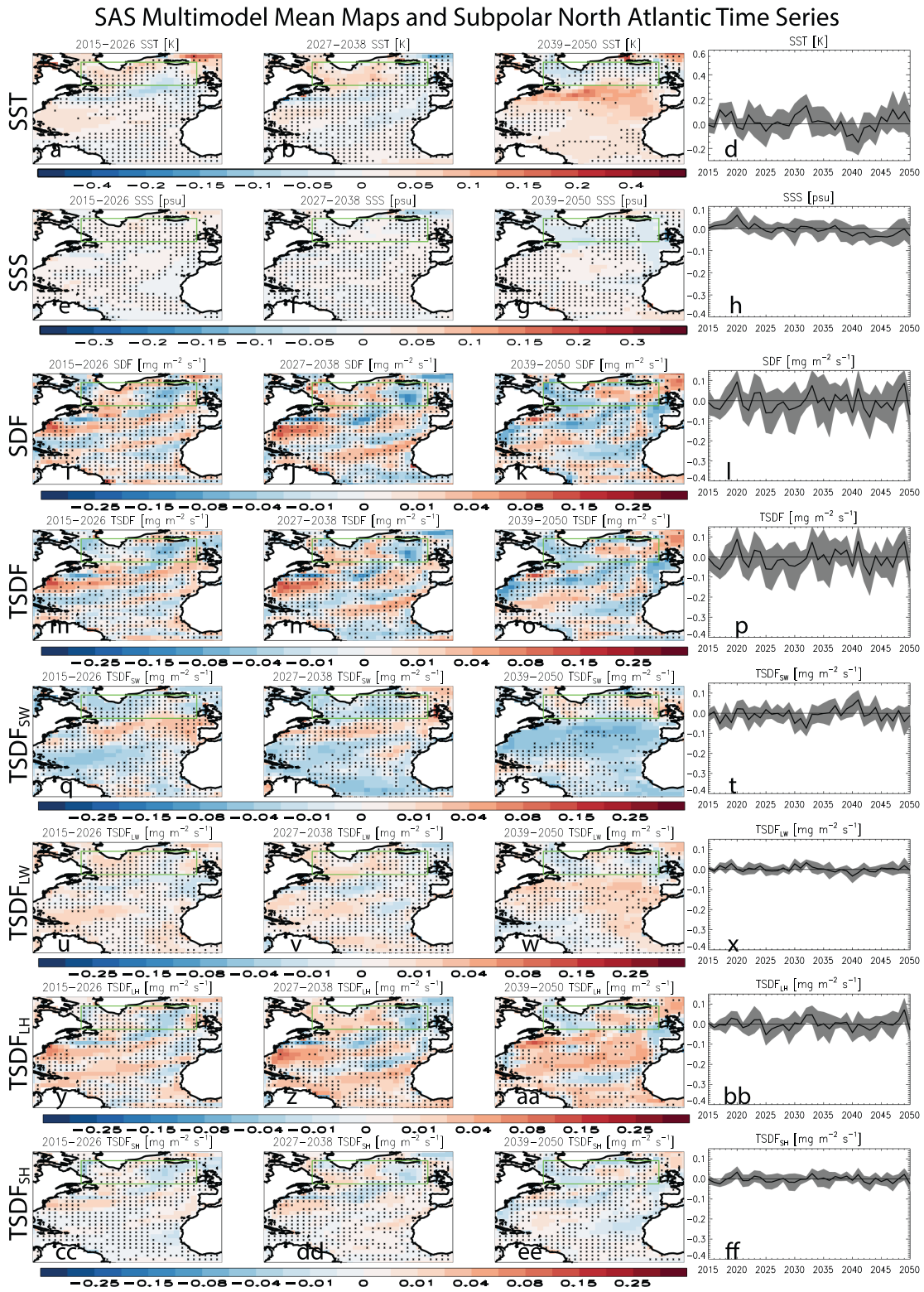

Figure 10. SAS multimodel mean maps and subpolar North Atlantic time series. Panels show responses for (a)–(d) sea surface temperature (K); (e)–(h) sea surface salinity (psu); (i)–(l) surface density flux (mg m^{-2} s^{-1}); (m)–(p) thermal component of SDF (mg m^{-2} s^{-1}); (q)–(t) shortwave radiation component of TSDF (mg m^{-2} s^{-1}); (u)–(x) longwave radiation component of TSDF (mg m^{-2} s^{-1}); (y)–(bb) latent heat component of TSDF (mg m^{-2} s^{-1}); and (cc)–(ff) sensible heat component of TSDF (mg m^{-2} s^{-1}). Responses are shown for three 12 year time periods including (a, e, i, m, q, u, y, cc) 2015–2026; (b, f, j, n, r, v, z, dd) 2027–2038; and (c, g, k, o, s, w, aa, ee) 2039–2050. Non-stippled regions indicate at least 6 of the 8 models agree on the sign of the response. Subpolar North Atlantic (green box) time series includes the uncertainty (gray shading), estimated as the 90% confidence interval across models.

3.3. AMOC responses beyond 2050

We briefly comment on the AMOC response to AA reductions beyond 2050. Two models, CESM2 and UKESM1-0-LL, extended their RAMIP simulations through 2079. Both models show continued North Atlantic Ocean AOD decreases under all perturbations, with larger decreases from 2060–2079 relative to 2039–2050 in all cases except East Asia (supplementary table 3). Under global AA reductions, for example, CESM2 shows enhanced North Atlantic Ocean AOD decreases from -9.0 ± 0.6 10^{-3} during 2039–2050 to -9.7 ± 0.5 10^{-3} during 2060–2079. Similarly, UKESM1-0-LL yields corresponding AOD decreases of -16.5 ± 0.9 10^{-3} and -18.9 ± 0.7 10^{-3}, respectively. Continued (and in most cases enhanced) reductions in North Atlantic Ocean AOD would be expected to drive continued weakening of the AMOC. In fact, Hassan *et al* (2021) shows that continued AMOC weakening beyond 2050 would be expected even if AOD anomalies do not continue to grow, because of a ∼10 year delay of the AMOC response to AOD. Post-2050 AMOC weakening occurs for CESM2 (under all perturbations) but less so for UKESM1-0-LL. Under CESM2, global AA reductions yield enhanced AMOC weakening (nearly a doubling) from -1.8 ± 0.18 Sv during 2039–2050 to Sv during 2060–2079. Similarly, AMOC weakening more than doubles from 2039–2050–2060–2079 for East Asia, Africa + Middle East and North America + Europe AA reductions (supplementary table 3). Although UKESM1-0-LL also shows similar enhanced AMOC weakening under global AA reductions (92% larger weakening from 2060–2079 relative to 2039–2050), minor changes occur for the four regional perturbations. This difference is consistent with the fact CESM2 exhibited a relatively large AMOC response over our default time period of 2015–2050, whereas UKESM1-0-LL did not (e.g. figure 3). As discussed above, some of this intermodel difference is related to their AMOC climatology (e.g. figure 5), but other factors also likely contribute and warrant further investigation (e.g. relative importance of the AMOC-salt advection feedback).

4. Discussion and conclusions

Using RAMIP experiments, which compare an SSP3-7.0 (weak levels of air quality control) to an SSP1-2.6 (strong levels of air quality control) aerosol emission pathway, we have quantified the impact of global and regional aerosol reductions on the AMOC by mid-century (figure 2). GLO (figure 3(a)) yields the largest multimodel AMOC weakening at-0.98 ± 0.40 Sv by 2039–2050, with all 8 models yielding a decrease. NAE (figure 3(b)) yields the second largest multimodel mean AMOC weakening at -0.34 ± 0.18 Sv with 7 of the 8 models agreeing on a decrease. AFR (figure 3(c)) yields the next largest weakening at -0.22 ± 0.14 Sv with 7 of the 8 models yielding a decrease. This is followed by EAS (figure 3(d)) at -0.19 ± 0.18 Sv with 5 of the 8 models yielding a decrease and SAS (figure 3(e)) at -0.05 ± 0.13 Sv with 5 of the 8 models yielding a decrease. Assuming linearity, the sum of the AMOC weakening across the four regional perturbations represents the bulk (82%) of that under global AA reductions. In other words, AA emissions reductions for the rest-of-the-world account for a small percentage of the total weakening at 12%. This is consistent with the aerosol ERF, as most of the rest-of-the-world forcing is in the Pacific (Allen *et al* 2026).

The multimodel mean AMOC response (2039–2050) across experiments is consistent with the North Atlantic Ocean aerosol ERF (from fSST simulations), where $r = -0.95$ (figure 4(a)). Thus, aerosol perturbations that feature larger positive North Atlantic ERF are associated with larger AMOC weakening. A similar (but positive) correlation occurs between the AMOC response and North Atlantic Ocean AOD from coupled simulations ($r = 1.0$). We note that from a global perspective, AFR yields the weakest global mean aerosol ERF at 0.05 ± 0.07 W m^{-2}, as compared to EAS, NAE and SAS with corresponding values of 0.15 ± 0.07 W m^{-2}, 0.13 ± 0.09 W m^{-2} and 0.10 ± 0.05 W m^{-2}, respectively (Allen *et al* 2026). Thus, it is the regional forcing (and the subsequent warming) as opposed to the global forcing that matters here. This is particularly evident for AFR, which has the second largest AMOC weakening, the smallest increase in global mean ERF, but the second largest increase in North Atlantic ERF.

All perturbations show a relatively large intermodel spread in AMOC response (e.g. figure 3). The intermodal spread in North Atlantic aerosol ERF does not consistently correlate to the corresponding intermodel AMOC spread (only GLO and NAE yield significant negative correlations). However, consistent with prior findings from CMIP6 (Weijer *et al* 2020), the intermodel AMOC spread in our simulations is related to each model's AMOC climatology (figure 5). Models that feature a stronger climatological AMOC are also associated with stronger AMOC weakening (figure 5; corresponding correlations are significant for GLO, NAE and EAS).

A deeper exploration of the mechanisms (figures 6–10) shows that AMOC weakening under AA reductions is associated with decreases in subpolar North Atlantic SDF, which are initiated by decreases in $TSDF_{SW}$, consistent with the positive North Atlantic forcing under aerosol reductions. These AA

forced AMOC weakening responses are subsequently reinforced by the AMOC-salt advection feedback. In some models, AFR AA reductions involve excitation of a negative NAO-like pattern (supp. figure 7), which weakens the subpolar North Atlantic surface winds and reduces surface turbulent heat fluxes (supp. figure 8), contributing to AMOC weakening. This is the case for the four models that yield significant AMOC weakening under AFR, including CanESM5-1, MRI-ESM2-0, NorESM2-LM, UKESM1-0-LL (figure 3(c)). The other four models lack both this dynamical response and significant AMOC weakening under AFR.

In contrast to the idealized simulations of Liu *et al* (2024), we do not find evidence for an AMOC response to East Asia or South Asia AA reductions that is opposite that from the other perturbations. We also note EAS and SAS lack a NAO-like response (supp. figure 9), which is dissimilar from that found in Liu *et al* (2024). There, a negative NAO-like response occurred in response to an increase in Asian anthropogenic aerosols, which weakened surface winds and heat fluxes in the subpolar North Atlantic. These differences are likely related to the lack of realistic aerosol forcing in Liu *et al* (2024), as they perturb SW radiation by a relatively large amount to mimic aerosol changes, i.e. 10% change in solar insolation over East Asia and South Asia. For Asia, this means a lot of the aerosol forcing over the Pacific in RAMIP experiments, largely due to aerosol-cloud interactions (e.g. Samset *et al* 2025; Allen *et al* 2026), is not accounted for in Liu *et al* (2024). This difference may be a key modifier of the Rossby wave train. A similar dynamical pathway was also found by Li and Liu (2025), again using a relatively large and idealized forcing (i.e. 10×sulfate from PDRMIP simulations). About half of these PDRMIP simulations are concentration-based (as opposed to emissions-based), so they may suffer from the same shortcoming, i.e. lack of remote forcing, for example over the Pacific. Perhaps more fundamentally, the Rossby wave teleconnection may require a sufficiently strong forcing threshold (one that is not crossed using the more realistic and weaker aerosol forcings of RAMIP). According to Liu *et al* (2024), the 10% change in solar insolation (their idealized surrogate for an aerosol perturbation) results in an annual mean net radiative forcing of 30 W m^{-2} in the perturbation regions (i.e. East Asia and South Asia). Allen *et al* (2026) provides a comprehensive analysis of the RAMIP ERFs. The corresponding ERF in the RAMIP EAS perturbation (also annual mean over the EAS region) is 1.64 ± 1.36 W m^{-2}. We note that this forcing is in response to a relatively large decrease (75%) in EAS SO_2 emissions. SAS yields a corresponding ERF (annual mean over the SAS region) of 1.61 ± 1.0 W m^{-2}. Thus, the idealized aerosol perturbation in Liu *et al* (2024) is a factor of nearly 20× larger. This suggests the different responses shown here (i.e. lack of a strong negative NAO teleconnection) is related to the smaller and more realistic aerosol forcing in RAMIP.

In contrast to the remote mechanism found in the idealized studies discussed above, RAMIP experiments show significant changes in aerosol related quantities over the North Atlantic (e.g. ERF in figure 1 and AOD in **supp.** figure 1). Such changes drive an increase in North Atlantic surface SW radiation (and decreased SDF), North Atlantic SST warming, and AMOC weakening. This shows the ability of atmospheric circulation to transport aerosols to the North Atlantic, even when they originate from afar (e.g. EAS). Furthermore, the multimodel mean AMOC responses across RAMIP experiments significantly correlate with these North Atlantic aerosol metrics (e.g. ERF and AOD in figure 4). Thus, our analysis shows the importance of atmospheric aerosol transport to the North Atlantic, which impacts the local surface SW radiative flux and subsequently the AMOC (with turbulent heat fluxes also contributing later on).

Global AA reductions yield AMOC weakening ⅓ of that under the high-GHG SSP3-7.0 pathway. The similar magnitude of AMOC weakening across SSPs (Weijer *et al* 2020), despite large differences in their GHGs, is likely related to their different aerosol pathways (i.e. more aggressive AA reductions generally occur under the lower GHG pathways, which will promote AMOC weakening). Our results show that efforts to improve air quality, particularly in North America + Europe but also far away in East Asia, will contribute to future AMOC weakening.

Acknowledgment

We acknowledge support by the Center for Advanced Study in Oslo, Norway which funded and hosted the HETCLIF centre during the academic year of 2023/24. The NorESM simulations were enabled by resources provided by the National Academic Infrastructure for Supercomputing in Sweden (NAISS). We also acknowledge the following funding sources: Research Council of Norway Grant 324182 (CATHY; BHS, LJW, RJA, AMLE). Horizon Europe Grant 101137639 (CleanCloud; BHS, LJW, AMLE). National Science Foundation Grant AGS-2153486 (RJA). Natural Environment Research Council (NERC) grant TerraFIRMA NE/W004895/1 (LJW, PTG, STR). National Center for Atmospheric Science, UK (LJW,

STR, SA). Environment Research and Technology Development Fund (JPMEERF20232001) of the Environmental Restoration and Conservation Agency provided by Ministry of the Environment of Japan (TK, NO). Arctic Challenge for Sustainability 3 (ArCS-3), Program Grant Number JPMXD1720251001 (TK, NO). Global Environmental Research Coordination System from the Ministry of the Environment of Japan Grant MLIT2253 (TK, NO). H2020 Societal Challenges Grant No. 101003826 (JM, RM, DOD). Research Council Finland Grant No. 337552. (JM, RM, DOD). Columbia-Lamont Center for Climate and Life (DMW). Natural Sciences and Engineering Research Council of Canada (NSERC) (PK, LJF). Swedish Research Council through Grant Agreements No. 2022-06725 (AL, AMLE) and 2020–04158 (AMLE). The U.S. National Oceanic and Atmospheric Administration under award NA23OAR4310601 (GP). Environment Research and Technology Development Fund (JPMEERF21S12010) of the Environmental Restoration and Conservation Agency provided by Ministry of the Environment of Japan (TT). This work was also supported by the University of Reading Advancing the Frontiers of Earth System Prediction (AFESP) Programme [award number A3720200] (SA). Climate modeling at GISS is supported by the NASA Modeling, Analysis and Prediction program, and resources supporting this work were provided by the NASA High-End Computing (HEC) Program through the NASA Center for Climate Simulation (NCCS) at Goddard Space Flight Center.

Data Availability Statement

The RAMIP data that supports the findings of this study are available through the Centre for Environmental Data Analysis (CEDA) archive at: https://catalogue.ceda.ac.uk/uuid/4680fd74cf2244ba8476ed2617e3b41f/ (Wilcox 2026).

Supplementary data 1 available at: https://doi.org/10.1088/2752-5295/ae63ef/data1.

Conflict of interest

The authors declare that the research was conducted in the absence of any commercial or financial relationships that could be construed as a potential conflict of interest.

ORCID iDs

Robert J Allen 0000-0003-1616-9719
Wei Liu 0000-0001-5958-3739
Laura J Wilcox 0000-0001-5691-1493
Bjørn H Samset 0000-0001-8013-1833
Sharar Ahmadi 0000-0002-2754-4820
Annica M L Ekman 0000-0002-5940-2114
Maxwell T Elling 0000-0001-6091-809X
Luke Fraser-Leach 0009-0003-9452-5528
Paul Griffiths 0000-0002-1089-340X
James Keeble 0000-0003-2714-1084
Paul Kushner 0000-0002-6404-4518
Anna Lewinschal 0009-0000-9526-4524
Risto Makkonen 0000-0002-8961-3393
Joonas Merikanto 0000-0002-1145-2569
Pierre Nabat 0000-0001-7034-638X
Declan O'Donnell 0000-0002-2700-471X
Naga Oshima 0000-0002-8451-2411
Geeta Persad 0000-0003-4690-0867
Toshihiko Takemura 0000-0002-2859-6067
Kostas Tsigaridis 0000-0001-5328-819X
Knut von Salzen 0000-0002-2991-6181
Daniel M Westervelt 0000-0003-0806-9961
Taufiq Hassan 0000-0003-2361-6361

References

Allen R J *et al* 2020 Climate and air quality impacts due to mitigation of non-methane near-term climate forcers *Atmos. Chem. Phys.* **20** 9641–63

Allen R J *et al* 2021 Significant climate benefits from near-term climate forcer mitigation in spite of aerosol reductions *Environ. Res. Lett.* **16** 034010

Allen R J 2025 *CESM2 Output Prepared for the Regional Aerosol Model Intercomparison Project (RAMIP)* (NERC EDS Centre for Environmental Data Analysis) (available at: https://catalogue.ceda.ac.uk/uuid/b7c87e4dafcc486ba1eca2abac752abf)

Allen R J *et al* 2026 Decomposing the global and regional aerosol effective radiative forcing associated with strong versus weak air quality policies by Mid-21st Century *Environ. Res. Clim.* **5** 025014

Allen R J, Vega C, Yao E and Liu W 2024 Impact of industrial versus biomass burning aerosols on the Atlantic Meridional Overturning Circulation *npj Clim. Atmos. Sci.* **7** 58

Bellouin N *et al* 2020 Bounding global aerosol radiative forcing of climate change *Rev. Geophys.* **58** e2019RG000660

Booth B, Dunstone N, Halloran P, Andrews T and Bellouin N 2012 Aerosols implicated as a prime driver of twentieth-century North Atlantic climate variability *Nature* **484** 228–32

Buckley M W and Marshall J 2016 Observations, inferences, and mechanisms of the Atlantic meridional overturning circulation: a review *Rev. Geophys.* **54** 5–63

Cheng W, Chiang J C H and Zhang D 2013 Atlantic Meridional Overturning Circulation (AMOC) in CMIP5 Models: RCP and historical simulations *J. Clim.* **26** 7187–97

Danabasoglu G *et al* 2020 The Community Earth System Model Version 2 (CESM2) *J. Adv. Model. Earth Syst.* **12** e2019MS001916

Delworth T L and Dixon K W 2006 Have anthropogenic aerosols delayed a greenhouse gas-induced weakening of the North Atlantic thermohaline circulation? *Geophys. Res. Lett.* **33** L02606

Delworth T L, Ramaswamy V and Stenchikov G L 2005 The impact of aerosols on simulated ocean temperature and heat content in the 20th century *Geophys. Res. Lett.* **32** L24709

Deser C, Alexander M A, Xie S-P and Phillips A S 2010 Sea surface temperature variability: patterns and mechanisms *Annu. Rev. Mar. Sci.* **2** 115–43

Diao C, Xu Y and Xie S-P 2021 Anthropogenic aerosol effects on tropospheric circulation and sea surface temperature (1980–2020): separating the role of zonally asymmetric forcings *Atmos. Chem. Phys.* **21** 18499–518

Eyring V, Bony S, Meehl G A, Senior C A, Stevens B, Stouffer R J and Taylor K E 2016 Overview of the Coupled Model Intercomparison Project Phase 6 (CMIP6) experimental design and organization, *Geosci. Model Dev.* **9** 1937–58

Forster P *et al* 2021 The Earth's energy budget, climate feedbacks, and climate sensitivity *Climate Change 2021: The Physical Science Basis. Contribution of Working Group I to the Sixth Assessment Report of the Intergovernmental Panel on Climate Change* eds V Masson-Delmotte *et al* (Cambridge University Press) pp 923–1054

Fox-Kemper B *et al* 2021 Ocean, cryosphere and sea level change in Climate Change 2021 *The Physical Science Basis* ed V Masson-Delmotte (Cambridge University Press) pp 1211–362

Fraser-Leach L, Kushner P, von Salzen K and Swart N 2025 *CanESM5-1 Output Prepared for the Regional Aerosol Model Intercomparison Project (RAMIP)* (NERC EDS Centre for Environmental Data Analysis) (available at: https://catalogue.ceda.ac.uk/uuid/a33a7cc2d0a84e27a78b24d70fe257e4)

Gregory J M *et al* 2005 A model intercomparison of changes in the Atlantic thermohaline circulation in response to increasing atmospheric CO_2 concentration *Geophys. Res. Lett.* **32** L12703

Hassan T, Allen R J, Liu W and Randles C A 2021 Anthropogenic aerosol forcing of the Atlantic meridional overturning circulation and the associated mechanisms in CMIP6 models *Atmos. Chem. Phys.* **21** 5821–46

Hassan T, Allen R J, Liu W, Shim S, van Noije T, Le Sager P, Oshima N, Deushi M, Randles C A and O'Connor F M 2022 Air quality improvements are projected to weaken the Atlantic meridional overturning circulation through radiative forcing effects, Commun *Earth Environ.* **3** 149

Lai W K M, Robson J, Wilcox L, Dunstone N and Sutton R 2025 The impact of model resolution of the North Atlantic response to anthropogenic aerosols *EGUsphere* 10.5194/egusphere-2025-2598 (preprint)

Lewinschal A 2025 *NorESM2-LM Output Prepared for the Regional Aerosol Model Intercomparison Project (RAMIP)* (NERC EDS Centre for Environmental Data Analysis) (available at: http://catalogue.ceda.ac.uk/uuid/44100d99d120487284d7b778dbc76bdf)

Li K-Y and Liu W 2025 Weakened Atlantic Meridional Overturning Circulation causes the historical North Atlantic Warming Hole *Commun. Earth Environ.* **6** 416

Li S, Liu W, Allen R J, Shi J-R and Li L 2023 Ocean heat uptake and interbasin redistribution driven by anthropogenic aerosols and greenhouse gases *Nat. Geosci.* **16** 695–703

Li X, Liu F, Luo Y, Zheng X-T and Wan X 2025 Evaluating the contribution of Asian aerosol emissions to the North Atlantic warming hole *J. Clim.* **38** 7187–202

Liu F, Li X, Luo Y, Cai W, Lu J, Zheng X-T, Kang S M, Wang H and Zhou L 2024 Increased Asian aerosols drive a slowdown of Atlantic Meridional Overturning Circulation *Nat. Commun.* **15** 18

Liu W, Fedorov A V, Xie S-P and Hu S 2020 Climate impacts of a weakened Atlantic Meridional Overturning Circulation in a warming climate *Sci. Adv.* **6** eaaz4876

Liu W and Fedorov A 2022 Interactions between Arctic sea ice and the Atlantic meridional overturning circulation in a warming climate *Clim. Dyn.* **58** 1811–27

Liu W, Fedorov A and Sévellec F 2019 The Mechanisms of the Atlantic Meridional Overturning Circulation Slowdown Induced by Arctic Sea Ice Decline *J. Clim.* **32** 977–96

Liu W and Liu Z 2013 A diagnostic indicator of the stability of the Atlantic meridional overturning circulation in CCSM3 *J. Clim.* **26** 1926–38

Liu W, Xie S-P, Liu Z and Zhu J 2017 Overlooked possibility of a collapsed atlantic meridional overturning circulation in warming climate *Sci. Adv.* **3** e1601666

Lund M T, Myhre G and Samset B H 2019 Anthropogenic aerosol forcing under the Shared Socioeconomic Pathways *Atmos. Chem. Phys.* **19** 13827–39

Ma X, Liu W, Allen R J, Huang G and Li X 2020 Dependence of regional ocean heat uptake on anthropogenic warming scenarios *Sci. Adv.* **6** eabc0303

Menary M B *et al* 2020 Aerosol-forced AMOC changes in CMIP6 historical simulations *Geophys. Res. Lett.* **47** e2020GL088166

Menary M B, Roberts C D, Palmer M D, Halloran P R, Jackson L, Wood R A, Müller W A, Matei D and Lee S-K 2013 Mechanisms of aerosol-forced AMOC variability in a state of the art climate model *J. Geophys. Res. Oceans* **118** 2087–96
Monerie P-A, Wilcox L J and Turner A G 2022 Effects of anthropogenic aerosol and greenhouse gas emissions on Northern Hemisphere Monsoon Precipitation: mechanisms and uncertainty *J. Clim.* **35** 2305–26
Mulcahy J P *et al* 2020 Description and evaluation of aerosol in UKESM1 and HadGEM3-GC3.1 CMIP6 historical simulations *Geosci. Model Dev.* **13** 6383–423
Nabat P 2025 *CNRM-ESM2-1 Output Prepared for the Regional Aerosol Model Intercomparison Project (RAMIP)* (NERC EDS Centre for Environmental Data Analysis) (available at: https://catalogue.ceda.ac.uk/uuid/5477e60b209a4e169ca60d7f01a017eb)
Needham M R, Falter D D and Randall D A 2024 Changes in external forcings drive divergent AMOC responses across CESM generations *Geophys. Res. Lett.* **51** e2023GL106410
O'Donnell D, Makkonen R and Merikanto J 2025 *EC-Earth3-AerChem Output Prepared for the Regional Aerosol Model Intercomparison Project (RAMIP)* (NERC EDS Centre for Environmental Data Analysis) (available at: https://catalogue.ceda.ac.uk/uuid/d581329422fb455ab9af0ea96c04d266)
Oshima N and Koshiro T 2025 *MRI-ESM2-0 Output Prepared for the Regional Aerosol Model Intercomparison Project (RAMIP)* (NERC EDS Centre for Environmental Data) (available at: https://catalogue.ceda.ac.uk/uuid/e8678aaf39144d8cb10cd02e8a562101)
Persad G *et al* 2023 Rapidly evolving aerosol emissions are a dangerous omission from near-term climate risk assessments *Environ. Res.: Clim* **2** 032001
Pincus R, Forster P M and Stevens B 2016 The Radiative Forcing Model Intercomparison Project (RFMIP): experimental protocol for CMIP6 *Geosci. Model Dev.* **9** 3447–60
Rahmstorf S 1996 On the freshwater forcing and transport of the Atlantic thermohaline circulation *Clim. Dyn.* **12** 799–811
Robson J, Menary M B, Sutton R T, Mecking J, Gregory J M, Jones C, Sinha B, Stevens D P and Wilcox L J 2022 The role of anthropogenic aerosol forcing in the 1850–1985 Strengthening of the AMOC in CMIP6 Historical Simulations *J. Clim.* **35** 6843–63
Rumbold S, Ahmadi S, Wilcox L, Keeble J, Griffiths P, Lister G and Predoi V 2025 *UKESM1-0-LL Output Prepared for the Regional Aerosol Model Intercomparison Project (RAMIP)* (NERC EDS Centre for Environmental Data) (available at: https://catalogue.ceda.ac.uk/uuid/63233813672245a2ba3c6de90c4cfaee/)
Samset B H *et al* 2016 Fast and slow precipitation responses to individual climate forcers: a PDRMIP multimodel study *Geophys. Res. Lett.* **43** 2782–91
Samset B H *et al* 2024 Broader research efforts and assessments needed to uncover the complex climate effects of regional changes in aerosol emissions *PLOS Clim.* **3** e0000508
Samset B H *et al* 2025 East Asian aerosol cleanup has likely contributed to the recent acceleration in global warming *Commun. Earth Environ.* **6** 543
Séférian R *et al* 2019 Evaluation of CNRM Earth-System model, CNRM-ESM2-1: role of Earth system processes in present-day and future climate *J. Adv. Model. Earth Syst.* **11** 4182–227
Seland Ø *et al* 2020 Overview of the Norwegian Earth System Model (NorESM2) and key climate response of CMIP6 DECK, historical, and scenario simulations *Geosci. Model Dev.* **13** 6165–200
Sellar A A *et al* 2019 UKESM1: description and evaluation of the U.K. Earth System Model *J. Adv. Model. Earth Syst.* **11** 4513–58
Stommel H 1961 Thermohaline convection with two stable regimes of flow *Tellus* **13** 224–30
Swart N C *et al* 2019 The Canadian Earth System Model version 5 (CanESM5.0.3) *Geosci. Model Dev.* **12** 4823–73
Takemura T 2025 *MIROC6 Output Prepared for the Regional Aerosol Model Intercomparison Project (RAMIP)* (NERC EDS Centre for Environmental Data) (available at: https://catalogue.ceda.ac.uk/uuid/7fbe5be720a34d4785cc7e3bb9df4641/)
Tatebe H *et al* 2019 Description and basic evaluation of simulated mean state, internal variability, and climate sensitivity in MIROC6 *Geosci. Model Dev.* **12** 2727–65
Textor C *et al* 2006 Analysis and quantification of the diversities of aerosol life cycles within AeroCom *Atmos. Chem. Phys.* **6** 1777–813
van Noije T *et al* 2021 EC-Earth3-AerChem: a global climate model with interactive aerosols and atmospheric chemistry participating in CMIP6 *Geosci. Model Dev.* **14** 5637–68
Weijer W, Cheng W, Garuba O A, Hu A and Nadiga B T 2020 CMIP6 models predict significant 21st century decline of the atlantic meridional overturning circulation *Geophys. Res. Lett.* **47** e2019GL086075
Wilcox L J *et al* 2023 The Regional Aerosol Model Intercomparison Project (RAMIP) *Geosci. Model Dev.* **16** 4451–79
Wilcox L 2026 Regional aerosol model intercomparison project *CEDA* (available at: https://catalogue.ceda.ac.uk/uuid/4680fd74cf2244ba8476ed2617e3b41f/)
Yukimoto S *et al* 2019 The meteorological research institute earth system model version 2.0, MRI-ESM2.0: description and Basic evaluation of the physical component *J. Meteorol. Soc. Jpn. II* **97** 931–965
Zhu T and Liu W 2025 Evolving Southern Ocean overturning in warming climates *Nat. Commun.* **16** 10449